

UNIVERSITY OF GRONINGEN

---

# The effect of temperature on hydrogen attachment to polycyclic aromatic hydrocarbons

---

*Author:*  
Arnold Dongelmans

*Examiners:*  
dr. Thomas Schlathölter  
prof. dr. ir. Ronnie Hoekstra

August 30, 2020

## Abstract

In this thesis, the theory and experimental set-up regarding hydrogenation of polycyclic aromatic hydrocarbons are explained. We aim to find the energy barrier of cororene  $C_{24}H_{12}$  by changing the temperature of hydrogen atoms that will attach to the cororene. By comparing the mass spectra obtained from theoretical models with our obtained experimental spectra for various temperatures, this is achievable.

# Contents

<b>1</b>	<b>Introduction</b>	<b>2</b>
1.1	Latest research and our contribution . . . . .	3
1.2	The interstellar medium . . . . .	4
1.2.1	Spectroscopy and categorization of the interstellar medium . . . . .	4
1.2.2	PAH formation in space . . . . .	5
1.2.3	Growth of PAHs . . . . .	7
1.2.4	Accretion of PAHs . . . . .	8
<b>2</b>	<b>Theory</b>	<b>10</b>
2.1	Kinetic theory equations . . . . .	10
2.2	Energy barrier of cororene . . . . .	11
2.3	Classical thermal physics . . . . .	13
2.4	Heat transfer . . . . .	14
2.4.1	Of the tube . . . . .	14
2.4.2	Flow inside the tube . . . . .	15
2.5	Collisions inside the tube . . . . .	15
2.6	Effusion . . . . .	17
<b>3</b>	<b>Experimental set-up</b>	<b>20</b>
3.1	Paultje . . . . .	20
3.2	The BalUn . . . . .	27
<b>4</b>	<b>Design</b>	<b>28</b>
4.1	Teflon tube encasing . . . . .	28
4.2	Thermal shrinking . . . . .	28
4.3	Heat flow of the encasing . . . . .	29
4.4	PID heat controller . . . . .	29
<b>5</b>	<b>Experimental results of attaching hydrogen and deuterium to PAHs</b>	<b>31</b>
5.1	Hydrogenation of cororene . . . . .	31
5.2	Deuteration of cororene . . . . .	34
5.3	Cascading flow . . . . .	36
5.4	Line broadening . . . . .	37
5.5	Extraction of the energy barrier . . . . .	37
<b>6</b>	<b>Conclusion and list of suggestions</b>	<b>42</b>
6.1	Points of improvements . . . . .	42
<b>7</b>	<b>Acknowledgements</b>	<b>42</b>
<b>A</b>	<b>Experimental techniques to determine adsorption energy and kinetic energy of H<sub>2</sub></b>	<b>46</b>

# 1 Introduction

Ever since ancient times we have been looking at the skies and wondered what is out there. Always relying on the visible spectrum by using our eyes and instruments like telescopes, we could partly make out what the universe looks like. Stars were relatively easy to spot and explain. The space in between stars is a different story; from data it can be inferred that there are dark patches where no light is emitted. Already in 1919, E. Barnard thought this was due to intervening opaque masses where light is absorbed. Not much later, in 1926 A. Eddington wrote in a paper that “In dark nebulae, atoms are mostly unionised, and there is no obstacle to the formation of molecules”. In places other than these dark patches, molecules might dissociate due to the interstellar radiation field and the subsequent atoms rarely join up again.

It was only with the advance of modern spectrometers we could look at the small constituents of this vast interstellar medium (ISM). An example is the Kuiper Airborne Observatory (KAO) which uses an arsenic-doped silicon detector to detect infrared emissions from the interstellar medium [1]. Many IR emission bands have been identified over the years, among which the -previously named-unidentified infrared emission bands (UIR bands) which are omnipresent in the ISM. The data was recorded and theories were thought of what could attribute to these findings. The IR-emissions from the Orion bar and NGC 7027 are depicted below in figure 1. It shows that peaks occur at vibrational modes of the PAH; regions denoted by the blue text. The hilltop capped off by the bold blue line is ascribed to (tens of) PAH clusters and to very small grains containing  $10^3 - 10^4$  C atoms. [2].

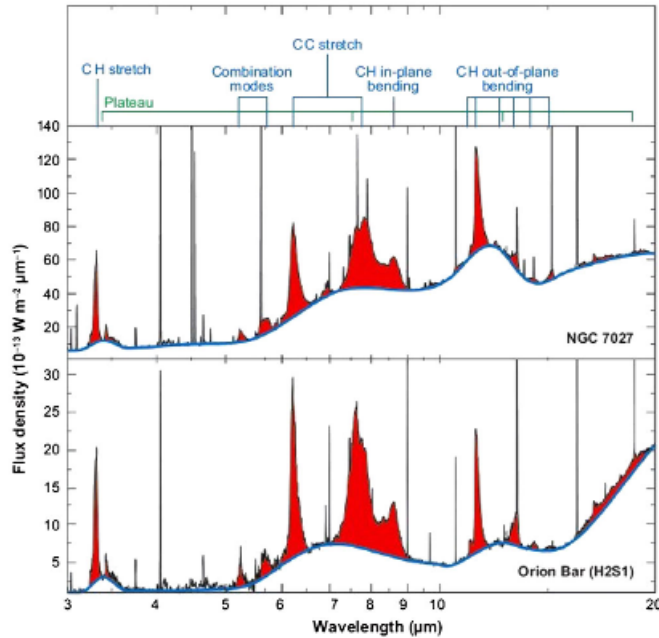


Figure 1: IR spectrum of the photodominant regions called the Orion bar and the planetary nebular NGC 7027.

Polyaromatic hydrocarbons (PAHs) are abundant throughout the interstellar medium, comprising about 20% of the interstellar clouds [3]. They may be an explanation of how molecular hydrogen is formed in the interstellar medium. It is therefore important to study the interaction, activation barrier and formation rate of PAHs.

## 1.1 Latest research and our contribution

The study of molecules in the interstellar medium is an interesting field. A method of studying them is by looking at their absorption and emission spectra. Large C<sub>60</sub> and C<sub>70</sub> molecules are confirmed to exist in space through their IR emissions [4]. The PAH hypothesis, that PAHs are the cause of the aromatic infrared bands, is generally accepted through studying emission spectra as well [5, 6]. Not only in the astrophysical/chemical world are PAHs of an interest but also in materials science: quantum dots [7], adsorption on graphene, [8] and the fabrication of thin films in optoelectronic applications [9]. Most related to this thesis is the work on how hydrogenation of PAH happens as a function of time. This was researched at the ZIAM in Groningen [10] and this thesis aims to expand upon that by studying the mass spectra of gas-phase cororene cations ( $C_{24}H_{12}^+$ ) with an number of attached hydrogen atoms. The hydrogen atoms will be cooled down via collisions with a cold Teflon tube up to -170°C, after which they will stick to the cororene. This has not been done experimentally before. Cororene is a relatively easy to come by PAH and highly stable, which is one of the reasons why this molecule is picked as the bigger the molecule, the higher the odds of capturing H in space. By analyzing the change in hydrogenation at different temperatures, the reaction barriers of cororene may be obtained.

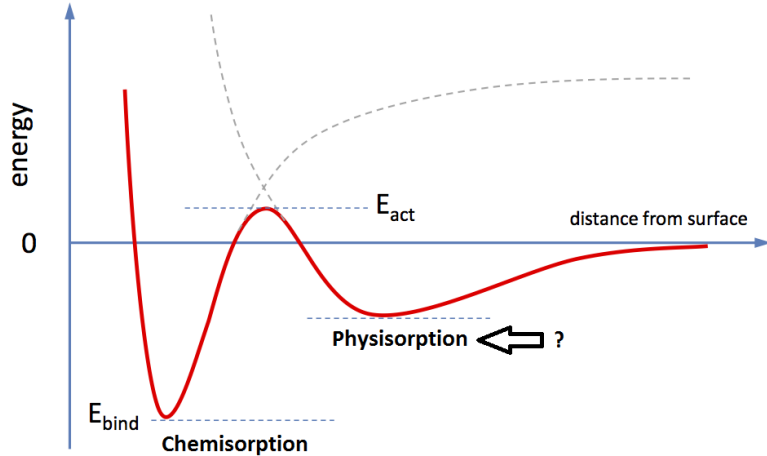


Figure 2: The physisorption barrier which ought to be found out.

## 1.2 The interstellar medium

### 1.2.1 Spectroscopy and categorization of the interstellar medium

As we want to know what the matter in between the stars is made of, we need emissions that we can detect from these places. There are 5 media as a subclass of the ISM. Hot ionized medium, warm ionized medium, warm neutral medium, atomic cold neutral medium and the molecular cold neutral medium, see figure 1.

The hot ionized medium is the hottest region and at its temperature of  $10^6\text{K}$  atoms within collide with each other and are able to rip off electrons from their parent nuclei (ionization). This “coronal gas” is believed to come from supernovae explosions. Also called planetary nebulae (a misnomer as it has no link to planets), these regions can be mapped by their emitted X-rays. The X-rays are produced by interactions of ions with the high energy electrons, that is  $k_b T_e$  ionization energy plasma ion where  $e$  stands for electron. Warm ionized H regions are regions where a star has recently formed; these protostars emit UV-radiation that ionizes hydrogen (HII). HII stands for hydrogen that is ionized once, while HI is neutral hydrogen (using Roman numerals). Captured electrons by the hydrogen cascade towards the ground state, emitting energy according to the Balmer-series as will be explained later. As there are not many stars compared to the amount of ISM, most of the hydrogen in the universe is unionized. This neutral medium can be detected using HI tracers: one of these is the hyperfine line emission of hydrogen, that is the emission of a photon due to the spin-up spin-down energy difference. This can happen when a hydrogen atom meets another hydrogen atom or a free electron, just enough energy to flip the spin and then emit the famous 21cm wavelength radiation in flipping to the lower energy state. The cold neutral medium can be traced the same, but is much less prevalent in the ISM. Molecular clouds are regions where gravity has pulled together interstellar gas, forming a high density cloud. Useful tracers for molecular clouds are CO rotational lines ( $^{12}\text{CO}$ ,  $^{13}\text{CO}$  and  $\text{C}^{18}\text{O}$ ) by looking at the missing lines in the emission spectrum, i.e. the absorption.

It depends on which phase of the interstellar medium we want to chart to pick an appropriate tracer.

ISM component	Designation	Temperature (K)	Density ( $\text{cm}^{-3}$ )
Hot ionized medium	Coronal gas	$10^5 - 10^6$	$10^{-4} - 10^{-3}$
Warm ionized medium	Diffuse ionized gas (HII)	$10^4$	10
Warm neutral medium	Intercloud (HI)	$10^4$	$10^{-1}$
Atomic cold neutral medium	Diffuse clouds	$10^2 - 10^4$	$10 - 100$
Molecular cold neutral medium	Molecular clouds	< 50	$10^3 - 10^5$

Table 1: The 5 different phases of the ISM. Adapted from: [11].

What is important to note is that in the hot ionized medium, despite technically being HI, it is quite different from the warm ionized medium. In the warm ionized medium, the ionization is an interplay between recombination and ionization by radiation e.g. UV. In the hot ionized medium, the plasma can be described by the ideal state Collisional Ionization Equilibrium (CIE). This model comprises the following:

1. Cooling.
  - Collisional ionization leads to cooling because it takes energy to ionize:  $A^c + e^- \rightarrow A^{c+1} + 2e^-(E_i)_A$ . Here  $c$  stands for charge,  $E_i$  the ionization energy and  $A$  the sample element. This is opposite to the hot ionized medium where a photoelectron is emitted, heating up the plasma.
  - Line cooling: the relaxation of a higher to lower energy state. This depends on the metallicity of the gas, as the metal line cooling is the most efficient way to cool up to

$10^6\text{K}$  [12]. Metallicity here means the percentage of the gas that has elements heavier than hydrogen, a term that has nothing to do with the technical meaning i.e. zero bandgap.

- Free-Free continuum cooling: when an electron passes close to an ion, it undergoes a deceleration. Particles undergoing deceleration emit radiation, thus the electron emits this. This radiation is called Bremsstrahlung, with energies typical to X-rays. This mechanism is dominant for  $T > 10^{6-7}\text{K}$  and is called free-free because the electron remains free *before* and *after* the interaction with the ion.

## 2. Heating.

- Supernova blast waves provide the main input of energy and momentum and is the dominant mechanism.
- Recombination is also a factor in heating the plasma, as this process favours slower electrons. This leaves the hotter electrons behind.

### 1.2.2 PAH formation in space

The absolute necessary ingredients for a PAH are hydrogen and carbon. H atoms formed about 3 minutes after the Big Bang, when the universe cooled to  $10^9\text{K}$  and when electrons stopped roaming freely [13]. Carbon is trickier to make as the temperature of the universe decreased too fast to initiate nuclear fusion. Instead, first a star needs to have formed to initiate this fusion. The first star is born about 200 million years after the Big Bang and starts the process to make carbon with the proton-proton chain (for  $4 \cdot 10^6\text{K} < T < 15 \cdot 10^6\text{K}$ ) by forming helium. Next, the helium fuses into carbon through the triple alpha process. In the lifetime of the star, more helium can be produced in the CNO cycle.

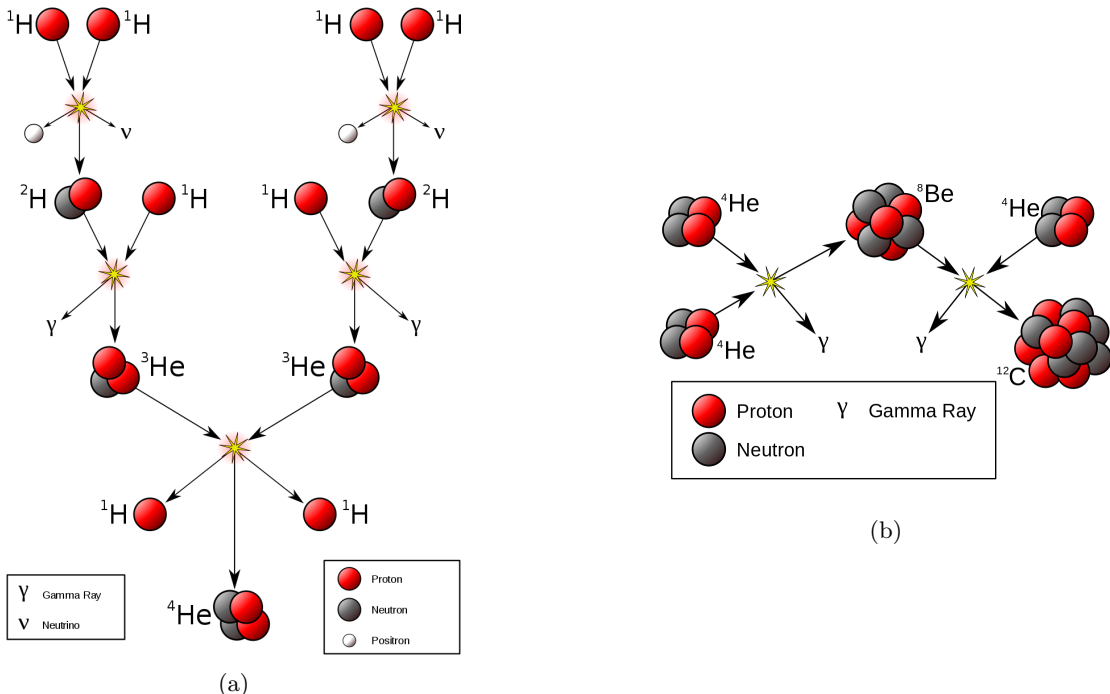


Figure 3: (a) In the proton proton chain, four protons start off and collide with each other and neutrons to form He. (b) In the triple alpha process  $2\text{He}$  fuse to form beryllium, a highly unstable element, which might fuse with another He before it decays to stable carbon.

PAHs are mainly formed due to outbursts from stars containing hydrogen and carbon. An example is in the vicinity of carbon-rich AGB stars with  $<8(M_\odot)$ . AGB stands for asymptotic giant branch and signifies the state after which the star has no hydrogen left in the core to fuse (resulting in a pure helium core). As fusion no longer takes place, there is no thermal pressure counteracting the gravitational pull of its own mass. The contracting star will keep shrinking until it is compressed enough to make the helium degenerate matter (obeying Pauli's exclusion principle). This comes with a degeneracy pressure which stops the very centre part of the star from contracting. The temperature keeps increasing while the star shrinks. At a temperature of around  $10^8 K$  the helium ignites and a thermal flash is emitted. This pulse comprises elements that are present in the star. In the case of our example star, late in its life cycle, the core consists mostly of carbon and oxygen. This can be ejected out into space via either strong winds or as in the form of a supernova. However, stars with a mass  $>8(M_\odot)$  will *fuse carbon* late in their life and are not a candidate for shedding the necessary elements for PAHs. The elements that are now floating in space will stick together to form so called diffuse clouds.

The next step is to combine the two aforementioned atoms to create the ingredient needed for PAHs, the CH molecule. Only very recently, the Herschel Space observatory obtained data that led to the conclusion that C atoms can bind to H atoms with the help of far UV-radiation (FUV, 6-13.6 eV) from young stars [14] as will be explained in the next paragraph. This happens in photodominated regions (PDRs), volumes in space filled with neutral gas that are hit by FUV. In these "clouds", dust grains are present which act as a catalyst for two H to form  $H_2$  as in figure 4, a necessary ingredient to form CH. The dust grains, officially called star dust, come from the mass ejections of stars and consist out hydrogen, nitrogen, oxygen and carbon. So,  $H + H + \text{grain} \rightarrow H_2 + \text{grain}$ , where part of the energy is absorbed by the grain and emitted as IR as in figure 4. One might ask why we need this reaction at all. This is because if on the rare occasion that 2 H atoms meet in the sparsely populated universe, they do not have enough contact time to emit a photon with the needed energy of 4.5eV to render the formed molecule stable. The contact time of the vibrational oscillation is only  $10^{-13}s$  while the transition probability is about  $10^{-8}s^{-1}$  [15]. This means you only have one vibrational period before the two H atoms part. On the grain, all the atomic H has to do is to wait for another H. The atomic H can either move to another physisorption site or move perpendicularly to the grain to a chemisorption site. Naturally  $H_2$  formation is easier when two physisorbed H atoms meet, rather than chemisorbed + physisorbed. Hence,  $H_2$  formation is higher for higher temperatures. But if the temperature high enough such that the H atom exceeds the threshold of desorption, the atom may "evaporate" of the grain. Once  $H_2$  has formed, it can easily escape the grain as the desorption energy is much lower now: it now needs less thermal energy, supplied by the grain, to desorb.

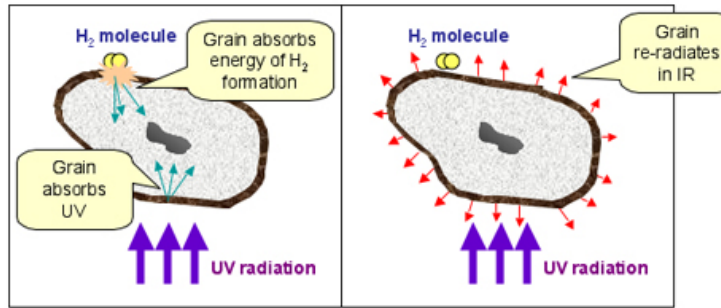


Figure 4: How grains absorb and radiate energy. Source: [16].

Naturally, the formation rate of  $\text{H}_2$  ( $\text{cm}^{-3}\text{s}^{-1}$ ) is dependent on many parameters and given by:

$$R_{\text{H}_2} = \frac{1}{2} n_H \nu_H A n_g S_H \gamma \quad (1)$$

where  $n_H$  is the gas number density,  $\nu_H$  the H atoms' speed,  $A$  the cross-sectional area of the grain,  $n_g$  the dust number density,  $S_H$  the sticking probability and  $\gamma$  the surface reaction probability to form  $\text{H}_2$  out of  $2\text{H}$  [17].

The other ingredient necessary, carbon, gets ionized by the high energy photons in these regions:  $\text{C} + \nu \rightarrow \text{C}^+ + \text{e}$  [18]. To combine C and  $\text{H}_2$ , an energy barrier of 0.36eV has to be bridged [19]. The main contributor to this abridging comes from the vibrational & rotational excitation of the  $\text{H}_2$  by photons from the hot, young star. The FUV ionized  $\text{C}^+$  molecules form up with  $\text{H}_2$  to produce  $\text{CH}_2^+$ , subsequently more  $\text{H}_2$  will join to form  $\text{CH}_3^+$  which can devolve into  $\text{CH}_2$ ,  $\text{CH}$  &  $\text{C}$  through dissociative electron recombination. A more obvious route would be  $\text{C}^+ + \text{H} \rightarrow \text{CH}^+ + h\nu$ . However, this radiative association has a rate coefficient which is orders of magnitude too low to explain the level of  $\text{CH}^+$  in molecular clouds. [20]. Another direct pathway is  $\text{C}^+ + \text{H}_2 \rightarrow \text{CH}^+ + \text{H}$  but this process is very endothermic, requiring a temperature of 4600K [19].

### 1.2.3 Growth of PAHs

There are essentially two ways to form PAHs in space; the bottom-up method, which was partly unveiled in section 1.2.2 and the top-down method. In the bottom-up method, the hydrocarbon needs some kind of radical site to allow for easier attachment of incoming atoms/molecules. The most dominant pathway on Earth [21] is the recombination of two  $\text{C}_3\text{H}_3$  radicals to form  $\text{C}_6\text{H}_6$  as depicted in figure 5, a closed ring structure [22].

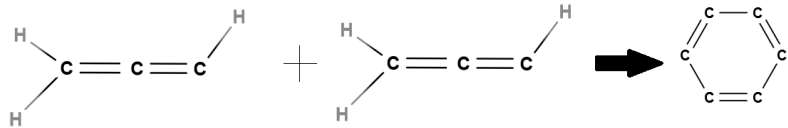


Figure 5: Combination into the first closed ring.

Now that the first ring has formed, the compound is aromatic i.e. a stable conjugated (p-orbitals) compound and it is much less able to react with other elements. The first ring forms the basis on which longer chains can grow.

However, there are many more pathways to form the first ring. This depends on which and how much of the reactant is present in the immediate surroundings of formation. For example, in the case of an abundance of  $\text{CH}_2$ , the reaction  $\text{CH}_2 + \text{C}_2\text{H}_2 \rightarrow \text{C}_3\text{H}_3 + \text{H}$  takes place after which the first benzene ring can form [23]. If  $\text{C}_4\text{H}_4$  is more abundant, it will form  $\text{C}_4\text{H}_3$  and  $\text{C}_4\text{H}_5$  by interaction with atomic hydrogen. This way a reaction like  $\text{C}_4\text{H}_5 + \text{C}_2\text{H}_2 \rightarrow \text{C}_6\text{H}_6 + \text{H}$  will yield the same final product, a closed ring.

The growth of the closed ring hydrocarbon also has different pathways. A well known one is the HACA mechanism; hydrogen abstraction-acetylene addition [24]. As the name hints, the sequence starts with an abstraction of a hydrogen atom (by another hydrogen atom) from the hydrocarbon after which an acetylene molecule ( $\text{C}_2\text{H}_2$ ) attaches to a radical site. After running this sequence twice, the simplest PAH naphthalene  $\text{C}_{10}\text{H}_8$  forms. Further HACA will eventually form cororene, the molecule investigated in this thesis. The temperature needed to attach the  $\text{C}_2\text{H}_2$  is 1100K meaning that this can only happen in outbursts from young stars or other hot regions [25].

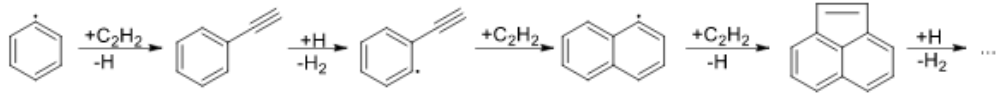


Figure 6: The HACA mechanism. Source: [23].

#### 1.2.4 Accretion of PAHs

The ISM is a harsh place for molecules to form due to the high UV radiation field, especially near young stars which have their photoemission peak at this wavelength. UV-radiation not only excites the PAHs to allow for detection via IR-emission but also destroys them if they are small enough. PAH are therefore mostly detected in molecular clouds where they are protected against this radiation. These are regions in space with a high concentration of molecules,  $>100\text{cm}^{-3}$ , and are ideal breeding grounds for long PAHs [26]. However, if the concentration of molecules is too high, the UV-absorption will not penetrate far into the cloud so not many PAHs can be observed besides the ones at the edge of the clouds. Molecular clouds themselves are a subclass of photodominant regions, PDRs, which are cold enough to remain neutral (more energy is needed to ionize) but not dense enough to stop UV-radiation from nearby stars.

These molecular clouds are the start region for star formation. This begins with the clustering into prestellar cores and infrared dark clouds. The first is characterized by a high density ( $3 \cdot 10^6\text{cm}^{-3}$  and a mass of  $(1\text{-}3)\text{M}_\odot$ ) [27]. The latter are dense molecular clouds but contain high-mass cores of  $120\text{M}_\odot$  instead of prestellar cores. Both are primarily detected using the CO rotational  $J = 1 - 0$  transition. Although  $\text{H}_2$  is much more predominant in clouds ( $10^5$  times more), CO is used as a tracer as the linear  $\text{H}_2$  has a much higher excitation energy ( $E_{\text{rot}} = 60.8J(J + 1)$  than CO ( $1.92J(J + 1)$  [28])) and is thus only visible in regions of high temperatures or regions of high radiation. The transition energies can be detected using instruments designed for that bandwidth of the electromagnetic spectrum as was done by ISO<sup>1</sup>, which used a spectrometer that covered the wavelength range of  $2.38 - 45.2\mu\text{m}$  with a spectral resolution ranging from 1000 to 2000 [29]. This way, molecular clouds can be traced.

As stated before, PAHs grow best in molecular clouds. However, the density of  $\text{C}_2\text{H}_2$  is much too low ( $3 \cdot 10^{-8}$  relative to  $\text{H}_2$ ) to have the HACA mechanism be the cause of further growth. Instead, PAHs accumulate on grains within the clouds. This dust comes from outflows of stars and can be silicate and oxides when the star has more oxygen than carbon, categorized as sand, or soot when the carbon outflow of the star is high. Young PAHs can settle on these grains and grow out to be a large family of complex species. The grains that are most stable do not fragment ( $>30\text{C atoms}$  [30]) when hit by UV radiation and can eventually cool down once the molecular cloud shields the inner dust grains enough. This is because the bigger the molecule the higher the vibrational degrees of freedom. This means the average energy absorbed (through a photon) per degree of freedom is lower which also lowers the probability of bond breaking [31]. More fundamentally; any system, according to thermodynamics, reaches its minimum energy by maximizing its entropy.

Once the grain has cooled enough, an ice mantle, dominated by frozen water and CO, forms which can trap attached elements. This can happen even at a low temperature of 10K. The atomic hydrogen quantum tunnels to move about, while heavier atoms like C and O hops thermally about the grain [32, 33]. This grain is now a factory for a variety of elements as UV-radiation and cosmic rays makes a plethora of chemical reactions possible as the elements trapped will get ionized. Once the molecular cloud accreted enough to collapse under its own gravity, a protostar forms. The subsequent heating will melt this ice and release the PAHs back into the gas phase.

The process discussed in this section has been summarized in figure 7 below.

<sup>1</sup>ISO stands for Infrared Space Observatory and was a project by ESA with the intention of mapping the infrared spectrum with a wavelength range of  $2.5$  to  $240\mu\text{m}$ .

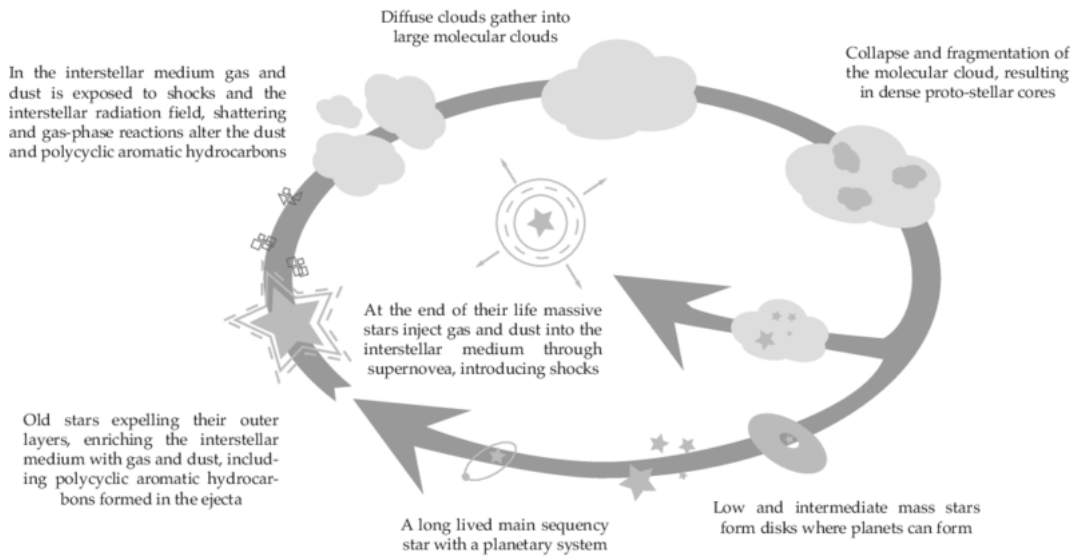


Figure 7: The recycling of dust in the ISM. Source: [34]

## 2 Theory

### 2.1 Kinetic theory equations

In order to study the energies, we have to employ kinetic theory: there are no other particle-particle interactions beside collisions. Several relationships are important to introduce such as the kinetic energy supplied to the hydrogen via temperature. We can use the following equation:

$$PV = \frac{1}{3}mv_{rms}^2 = \frac{1}{3}nMv_{rms}^2 \quad (2)$$

The above equation comes from the definition of pressure in the kinetic theory of an ideal gas, where  $m$  is the mass of the liquid/gas,  $M$  the molar mass and  $n$  the amount of moles. If we equate this to the gas law, we obtain  $v_{rms}$  as a function of temperature:

$$PV = NRT = \frac{1}{3}nMv_{rms}^2 \quad (3)$$

$$v_{rms} = \sqrt{\frac{3RT}{M}} \quad (4)$$

Another parameter that is important is the mean free path:

$$\lambda = \frac{1}{\sqrt{2}\frac{N}{V}\pi d^2} \quad (5)$$

where  $N$  is the number of molecules and  $d$  the diameter of the molecule. The  $\sqrt{2}$  comes from the fact that all molecules collide with each other; as each molecule has a standard deviation of  $v_d$ , two molecules have a standard deviation  $v_{2d} = \sqrt{v_d^2 + v_d^2} = \sqrt{2}v_d$ . Hence the effective speed is  $\sqrt{2}$  as big in this dynamic system.

Lastly, if we want to find out what fraction of particles lies in a certain interval  $v, v + dv$  we employ the well-known Maxwellian velocity distribution:

$$f_v = \left(\frac{m}{2\pi kT}\right)^{3/2} e^{-\frac{mv^2}{2k_b T}} \quad (6)$$

which holds for atoms and molecules in a 3D space configuration.

## 2.2 Energy barrier of cororene

The incoming hydrogen atom has to overcome a barrier to stick to cororene. This barrier has a theoretical value of 60meV [35] and allows the hydrogen to stick to the outer edge of the cororene molecule as in figure 9a. Several other sites are possible, depending on the energy of the incoming hydrogen atom. Up to 24 hydrogen atoms can stick to the molecule before all sites are occupied as shown in figure 8. The chemical equation for this (where  $s$  is the number of previously attached H atoms) is:

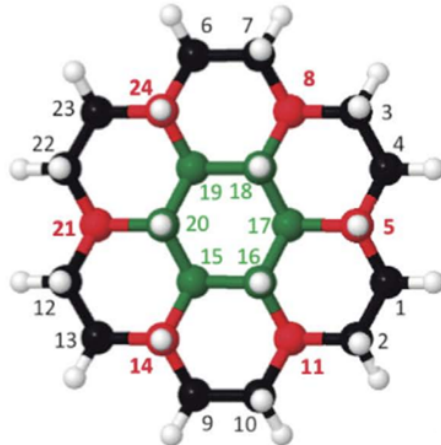
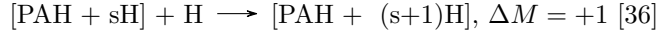
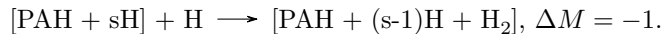


Figure 8: The possible sites for hydrogen attachment. Here the colorcoding black, red and green represent the outer edge, edge and center sites respectively. Source: [37].

After the first H attachment (with a binding energy of 1.45eV), the second H may land on a site next to the first outer edge site, the most favourable position due a low energy barrier (estimated 0-10meV), as shown in 9a. This second hydrogen atom will tilt the C-C bond which contributes to this attachment its binding energy of 3.25eV (figure 9b). The binding energy of two H atoms  $\approx 4.7\text{eV}$  ( $1.45\text{eV} + 3.25\text{eV}$ ) is higher (or deeper in the potential well) than the binding energy after they have formed  $\text{H}_2$ . Therefore it is not energetically favorable to form  $\text{H}_2$ , molecular hydrogen.

The cororene can also be dehydrogenated by means of an Eley-Rideal reaction [38]: the incoming hydrogen atom *may* take away a H atom, and take off to form  $\text{H}_2$ . This chemical equation is:



An example of this reaction is shown in figure 9c.

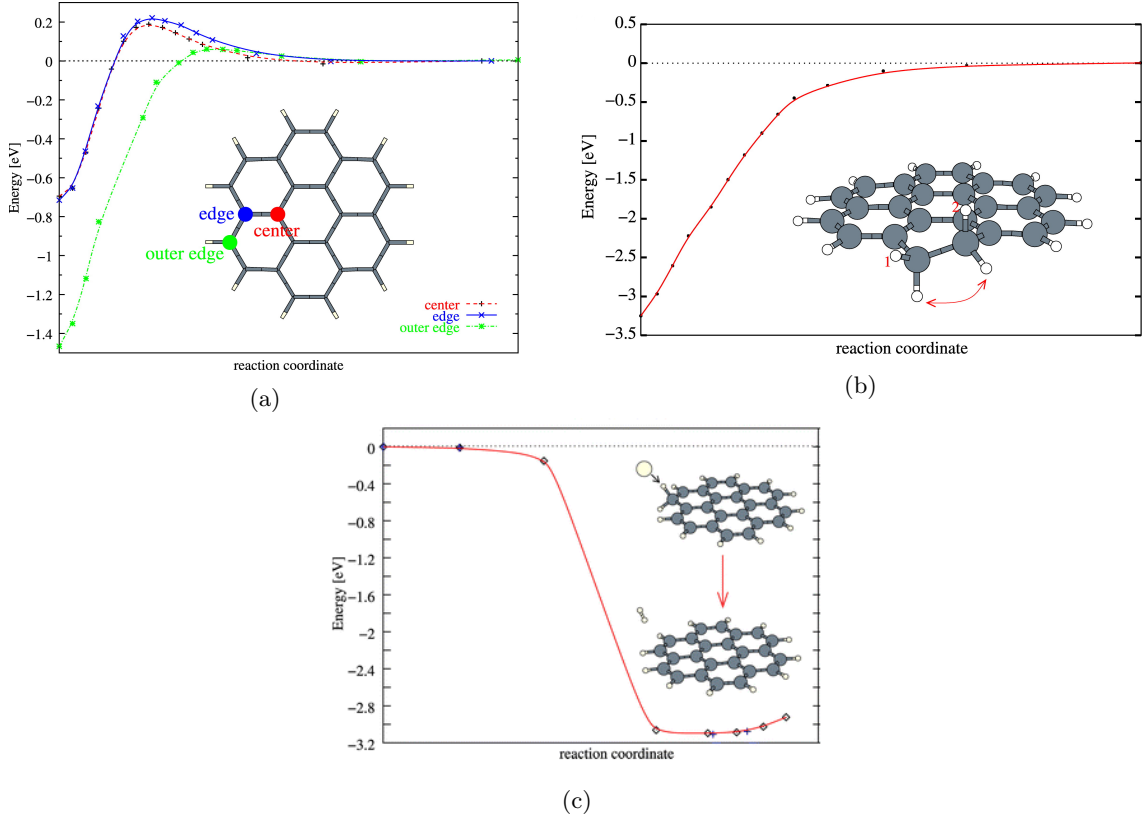


Figure 9: Potential energy barriers for hydrogen attachment to the outer edge (a) the first H (b) the second H. In (c), the potential energy curve is plotted of molecular hydrogen formation by a Eley-Rideal reaction, the second H atom taking away the first by directly impinging on it. Further sequences are illustrated in: [35].

What is important to note is that the energy barrier alternates from a low barrier to a higher barrier for an odd and even amount of already attached H atoms respectively, *if the cororene is neutral*. In the case of cororene cations, the opposite is true. This can be attributed to a spin-coupling i.e. an unpaired spin turns the system in a radical, making it react with other unpaired spins more easily. This allows the system to enter a lower energy state with an even amount of H atoms [10].

We can find out the kinetic energy of the hydrogen atoms that strike the cororene by using equation 3. This yields  $v_{rms} = 1578 m/s$  with corresponding energy of 0.013eV. To find out the energy barrier experimentally, we use the Arrhenius equation:

$$k = A e^{-\frac{E_a}{RT}} \quad (7)$$

where  $E_A$  is the activation energy (energy barrier)  $A$  the frequency factor and  $k$  the rate constant. By plotting the log of the rate constant versus  $\frac{1}{T}$  for different temperatures we can find out the energy barrier:  $\ln(k) = -(E_a/R)(1/T) + \ln A$  Now the slope of this graph would be  $-E_a/R$ . In the case of our theoretical model, we solve a set of time dependent differential equations. The different reactants and products are coupled and  $k$ , is constant (at a fixed T) because we do not change any other parameters. The way this is calculated will be further elaborated on in section 5.5.

## 2.3 Classical thermal physics

In the ISM, heat can only be transferred through radiation by and to any black/greybody. The sun emits about 50% of its energy as IR, 40% as UV and 10% in the visible wavelength spectrum. This energy might get absorbed by stable enough bodies, or destroy them. In the case of PAHs, the UV radiation populates the ground state of the vibrational levels, then decays radiationless to the ground electronic state after which infrared-emission cools the PAH radiatively, depicted in figure 10. Another means of dissipation is through Poincaré fluorescence [39].

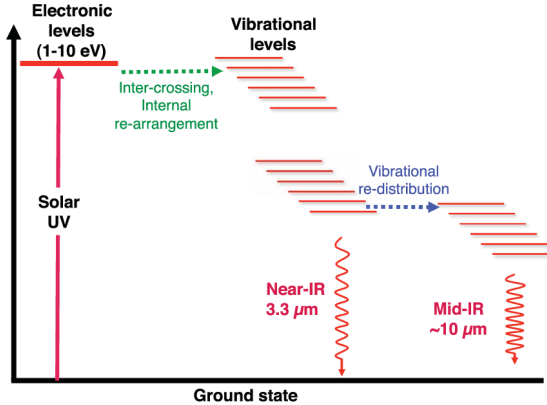


Figure 10: A schematic diagram, showing the absorption, relaxation and emission by PAHs. Source: [40].

Cooling in our set-up is done via a vessel of non-contact liquid nitrogen as will be explained in section 3. The cooling happens collisionally as the outer H atoms of flowing through a tube slow down when colliding with the cold wall. An important parameter here is the mean free path of hydrogen  $\lambda$ . For this we use equation 5. A plot is shown below in figure 11 for hydrogen, where the theoretical atomic diameter of H  $106 \cdot 10^{-12} m^2$  [41].

---

<sup>2</sup>106pm is the mean value calculated by solving the radial component of Schrödinger's equation and setting  $\frac{d\psi}{dr} = 0$  for the n=1, l=0 & m=0 (1s) wavefunction. This is the same result Niels Bohr calculated in the old planetary model. The radius remains ill-determined as quantum mechanics plays a role. The covalent radius is also often used in literature (74pm) which is the radius of one H atom upon forming a covalent bond with another H atom.

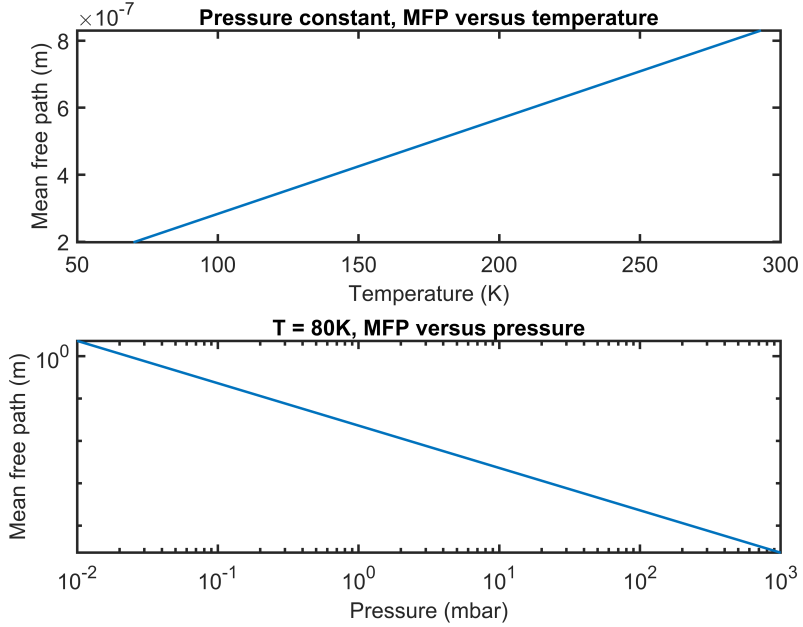


Figure 11: Mean free path for hydrogen.

As  $\lambda$  can be several centimeters for low pressures, it will also lose its energy via collisions more slowly than at higher pressures. For a pressure of  $10^{-4}$  mbar, the border between process and high vacuum at which many experiments operate, and a temperature of 100K,  $\lambda$  is already  $5.67\text{m}$ . We need to know if our flow is in the viscous flow regime or molecular flow regime. This can be found out through the Knudsen number:

$$Kn = \frac{\lambda}{d} \quad (8)$$

where  $d$  is the diameter of the fluid-vessel. If the Knudsen number is bigger than 0.5, the flow is in the molecular regime i.e. there is a negligible interaction between the particles. For a  $d$  of 14mm, our tube its diameter, this would happen at  $\lambda = 3.5 \cdot 10^{-3}\text{m}$ . A quick glance at figure 11 shows this happens at a pressure of  $\approx 10^2$  mbar. As our set-up operates at pressures well below that, we can conclude the particles interact more with the walls than with each other; the particles are in the molecular regime<sup>3</sup>.

## 2.4 Heat transfer

### 2.4.1 Of the tube

It takes time for the tube to thermalize; which, macroscopically, can be calculated via the heat conductivity of two media using Fourier's law:

$$q = -kA \frac{\partial T}{\partial r}$$

Solving this for a cylinder yields:

$$q = \frac{2\pi L(T_i - T_o)}{\ln(r_2/r_1)/k_{12}}. \quad (9)$$

---

<sup>3</sup>Note that even though called *molecular*, the flow does not necessarily have to consist out of molecules. *Atoms* can also be in the molecular regime

where  $q$  is the heat transfer in Watts,  $T_i$  &  $T_o$  the inner and out temperatures of the cylinder and  $k_{12}$  the heat transfer coefficient of the material in between the two boundaries. As  $L$  is the length, the heat transfer will scale linearly when one increases the cylindrical vessel. This can be solved numerically and the results for our specific experiment are given in section 4.3. An illustration how the heat transfer happens is shown in figure 12.

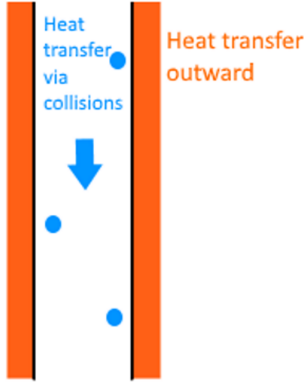


Figure 12: How the atomic hydrogen atoms get cooled. Blue signifies the atoms and the brown-orange color the solid that acts as a solid heat transfer block.

#### 2.4.2 Flow inside the tube

We need to determine the kinetic energy of the hydrogen atoms that will stick to the cororene. For atomic hydrogen there are no studies on how well it transfers heat in the molecular flow regime, so instead we have to check if the amount of collisions with the colder capillary walls is sufficient to thermalize. Luckily, the atomic hydrogen that exits the Teflon tube will not be heated up by any radiation with room temperature energies because the amount of energy needed to transit from the first orbital  $n = 1$  to the second  $n = 2$  is  $13.6\text{eV} - 3.4\text{eV} = 10.2\text{eV}$ , which is much higher than blackbody radiation from inside Paultje (our experimental set-up, see section 3), which peaks at  $1.28 \cdot 10^{-1}\text{eV}$  for an emitter at  $25^\circ\text{C}$ .

## 2.5 Collisions inside the tube

To make sure a particle makes a sufficient amount of collisions with the wall to cool down, we can simulate the flow using Molflow+<sup>4</sup>. The only inputs are the physical parameters of the gas and the outgassing rate (the industry standard, also known as the leak rate) with units  $\text{mbar} \cdot \text{l/s}$ . The atomic hydrogen flow can be converted from ml/sec to this outgassing rate by multiplying with a factor of 1.013 [43]. For a flow rate of 10% (0.5ml/min) of our flow controller's maximum of 5ml/min (of which the operating mechanism will be explained in section 3), this would be  $1.013 \cdot \frac{0.5}{60} = 0.0084 \text{ mbar} \cdot \text{l/s}$ . The result is shown in 13a. Note the higher pressure at the entrance just like in figure 14. In order to show the amount of particles that collide with the wall, COMSOL<sup>5</sup> is used. For the COMSOL simulation, the Teflon tube's exterior were set to “wall”, meaning no adsorption/desorption takes place as we are only interested in the incident flux. The inlet of these kind of simulations requires the flow in SCCM, standard cubic centimeters per minute. One can easily convert:  $1 \text{ SCCM} = 59.2 \cdot \text{mbar} \cdot \text{l/s}$ .

<sup>4</sup>A Monte-Carlo Simulator package developed at CERN to simulate molecular flows [42].

<sup>5</sup>COMSOL is a finite element analysis programme used to simulate and solve scientific and engineering problems based on partial differential equations [44].

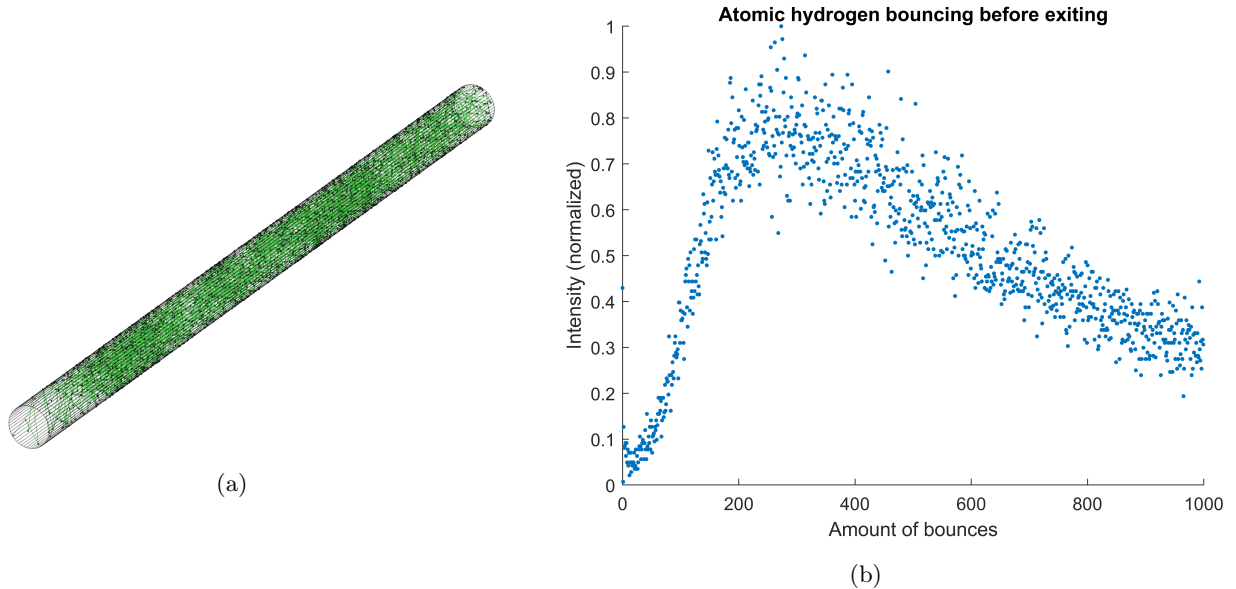


Figure 13: (a) A time snapshot of the trajectory of the atomic hydrogen inside the tube, reflecting many times before exiting. As this is no average of the total flow and Molflow+ can only draw 2048 lines per snapshot, this is a mere illustration of the ballistic bouncing. (b) The amount of bounces off the wall before exiting the tube.

Figure 14 shows the incident flux per second. The longer tube shows more collisions near its entrance due to its exit being farther away which decreases the pressure gradient. This causes the reflecting particles to strike the wall but reflect in a more diffuse away as opposed to the shorter tube.

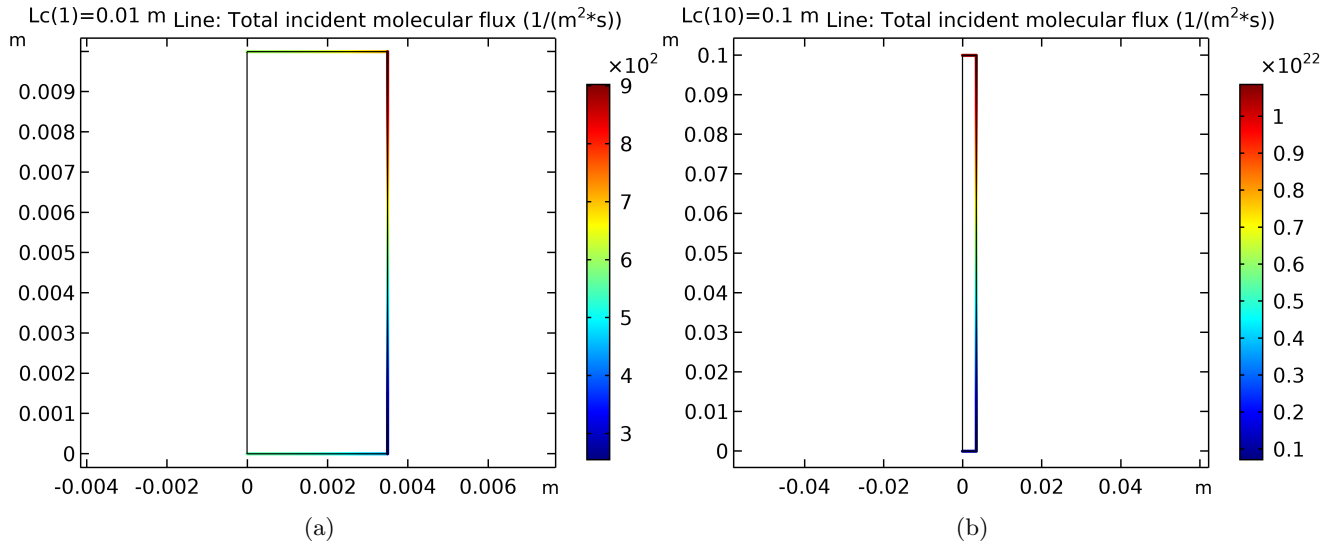


Figure 14: Flux of atomic H on the cylindrical Teflon tube entering from the top with a vacuum reservoir at the bottom. Left shows a tube length of 1cm and right 10cm.

## 2.6 Effusion

In order to find out the energy distribution of the atomic hydrogen emerging from the tube, to determine how energetic the atom is that hits the cororene, we utilize statistical mechanical calculations. Because the tube its diameter is so much smaller than  $\lambda$ , the particles do not emerge in an isotropic way, they have a preference in the direction parallel to the walls. Therefore we will have to modify the standard isotropical probability density function. The particles emerge from the tube its aperture, or opening, at the end. This process is called effusion.

Consider an aperture with area  $A$  on the perimeter of a closed tube filled with particles. The velocity distribution of particles with speed  $v_z$  is given by:

$$f_z(v_z) = \int \int f(v_x, v_y, v_z) dv_x dv_y = \sqrt{m/2\pi kT} e^{-mv_z^2/2kT} \quad (10)$$

The mean velocity in the z-direction can be calculated via:

$$\langle v_z \rangle = \int v_z f(v_z) dv_z \quad (11)$$

Next we calculate the impingement rate  $z$  in the z-direction

$$z = n \langle v_z \rangle = n \int v_z f(v_z) dv_z = n \sqrt{kT/2\pi m} \quad (12)$$

Using the ideal gas law:  $n = \frac{P}{kT}$

$$z = \frac{\Delta P}{\sqrt{2\pi mkT}} \quad (13)$$

which has dimensions of (exiting) particles per area per second, not to be confused with flux  $\Phi$  which does not take into account the time dimension. By multiplying with the area  $A$  of the aperture, one obtains the amount of molecules second [45]. However, this equation assumes a Maxwellian distribution, something we cannot use. We shall see later what we have to do to account for effusion.

Equation 13 has implicitly assumed that the particles can come from any direction. That means they could have collided within the tube before the aperture. If you want to calculate the amount of particles effusing through the hole without hitting the wall, you would need to integrate over different angles.

$$z_{hole} = nv_z f(v) d^3v = \int_0^\infty nv^2 \textcolor{blue}{v} f(v) dv \int_0^\theta \textcolor{red}{cos}\theta \sin\theta d\theta \int_0^{2\pi} d\phi \quad (14)$$

Here  $\theta$  is the angle between the normal of the aperture and the incoming particle,  $v_z = v \cos\theta$ ,  $d$  is the diameter of the aperture and  $l$  the length of the traversed path.  $\theta$  needs to be set such that it forms an as large as possible “cone” in the tube, without hitting the walls. Equation 14 is **not** isotropic (uniform in all directions) nor follows a Maxwell-Boltzmann velocity distribution, despite the gas before the entrance of the tube might. It is not isotropic because, just like a skipping stone more parallel to the water surface is more likely to reach further, for small  $\theta$ , the particles emerge with higher probability. This is what the added (compared to an isotropic probability density function)  $\textcolor{red}{cos}\theta$  is for. The extra  $\textcolor{blue}{v}$  makes the speed distribution (everything involving  $v$ ) extra sensitive to higher velocities.

The equation also shows that the smaller the diameter of the aperture (and hence the smaller the upper limit on the maximum angle before hitting a wall), the lower the flux. The upper limit of the angle can be quantified as  $\theta_{upper} = \tan^{-1}(\frac{d/2}{l})$ . It is maximum for  $\theta = \pi/2$  as  $v_z = v \cos\theta > 0$  signifies particles moving towards the aperture. Integrating equation 14 for  $\theta = \pi/2$  &  $\phi = 2\pi$  would yield equation 13 again.

If we only care about the velocity distribution and not the amount of particles we would only need to integrate over the angles:

$$f(v)_{angle} = nv^3 f(v) dv \int_0^{\pi/2} \cos\theta \sin\theta d\theta \int_0^{2\pi} d\phi = \pi nv^3 f(v) dv = \frac{1}{4} nv \bar{f}(v) dv \quad (15)$$

where  $\bar{f}(v) = 4\pi v^2 f(v)$  [46]. The number density,  $n$ , can be extracted from the ideal gas law, assuming  $P = 10^{-6}$  mbar &  $T = 300K$ ;  $\frac{n}{V} = \frac{P}{RT} = 2.41 \cdot 10^{10}$  atoms/cm<sup>3</sup>. For hydrogen atoms, this would look like figure 15.

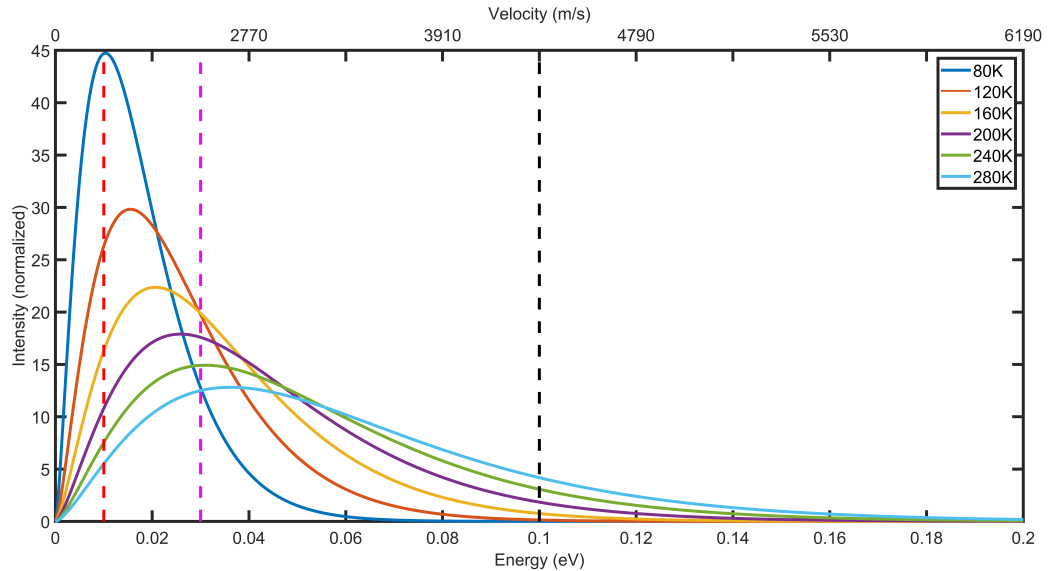


Figure 15: The energy distribution of the molecular flow exiting the Teflon tube. The dashed lines indicate energy barriers for several H additions: red for 0.01eV, magenta for 0.03eV and black for 0.1eV. See 5.5.

To calculate the fraction of the distribution that overcomes the physisorption barrier, you calculate equation 14 for  $\int_{v_{barrier}}^{\infty}$ . This gives the following result:

	Fraction overcoming barrier at 80K	120K	160K	200K	240K	280K
Energy barrier of 0.01eV	0.57	0.75	0.84	0.88	0.91	0.93
Energy barrier of 0.03eV	0.07	0.21	0.36	0.48	0.57	0.65
Energy barrier of 0.1eV	7.81e-06	6.75e-04	5.85e-03	0.02	0.05	0.08

Table 2: Fraction of H atoms overcoming energy barriers.

If we want to know the amount of particles that move straight through the tube, without any collisions with the wall and hence no thermalization, we would need to know  $\theta_{upper}$ , the highest angle without collisions and  $n$ , the number density which was calculated before ( $2.41 \cdot 10^{10}$  atoms/cm<sup>3</sup>). For a tube with  $d = 0.0032m$  &  $l = 0.1$ ,  $\theta_{upper} = 0.016rad$ .

Then, using equation 6 for  $f(v)$ , integrating equation 14 for  $\theta = \theta_{upper}$  &  $n = 2.41 \cdot 10^{10}$  atoms/cm<sup>3</sup> will yield the amount of particles exiting the tube. Compared to the amount of particles that move about in any direction, albeit downward so  $\theta = \pi/2$ , the  $\theta_{upper}$  restriction makes it so that only about 0.001% makes it through without a collision. This is due to the contribution of the integral  $\int_0^{\theta_{upper}} \cos(\theta) \sin(\theta) d\theta$ . The angular distribution is show in figure 16.

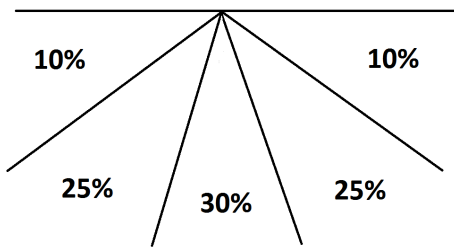


Figure 16: The angular distribution for a molecular flow.

### 3 Experimental set-up

#### 3.1 Paultje

We use the “Paultje”, a home-built tandem mass spectrometer to study the composition and fragmentation of molecules. Currently, Paultje consists out of an electrospray acting as the ion source, a quadrupole acting as mass filter, an octopole acting as ion guide, the Paul trap, a reflectron and a mass detector. A schematic is shown in figure 17. Paultje will be explained from left to right on this schematic.

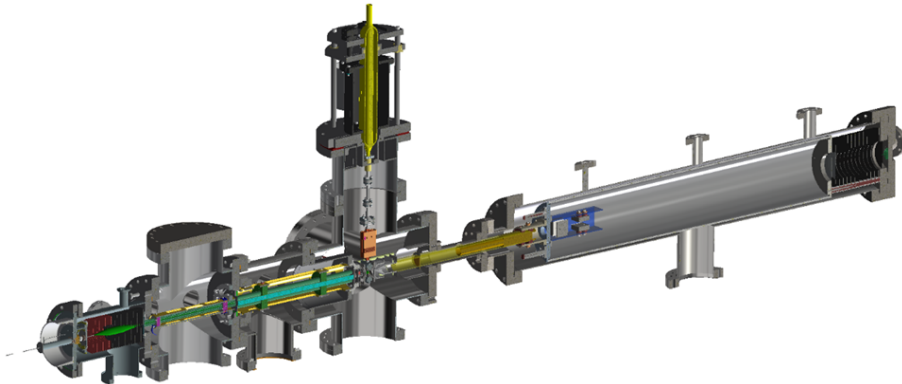


Figure 17: The experimental set-up.

The ions to be investigated enter Paultje through the electrospray: the electrospray stage consists out of a syringe containing the ions in a solution and a needle at a high potential of 3 to 3.5kV. We use a solution that consists out of  $25\mu L$  of 10mM of  $\text{AgNO}_3$ ,  $225\mu L$  of HPLC-grade methanol and  $250\mu L$  of methanol saturated with cororene. The saturated cororene solution is made by filling a test tube with cororene up till the 0.3ml line and adding 0.7ml of methanol. After this the test tube is spun in a centrifuge and a small volume of the saturated solution can be skimmed off from the top. Once the solution is complete, it is drawn up by a syringe in order to supply it to the ESI stage. A tubing, designated for the highly contaminating PAHs, delivers the solution to a needle. A potential difference between the needle and capillary makes the molecules traverse the gap in between. As the droplet exits the needle, the solvent evaporates due to heat supplied to the tip of the needle. The droplet decreases in size until the increase in electric field density increases the surface tension to a point where the droplet fissions due to charge repulsion, called the Rayleigh limit. The ions that enter the next stage can be negatively or positively charged, depending on what exited the needle. In our case of cororene cations, they are positive.

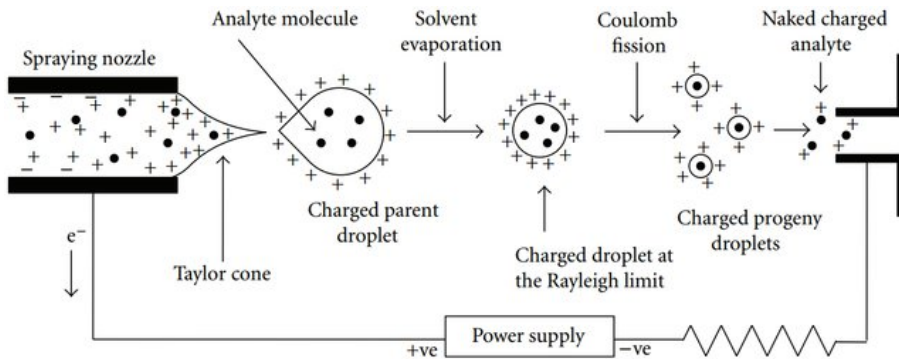


Figure 18: Schematic of an electrospray configuration. Source: [47].

The next stage is the ion funnel. The ion funnel acts to focus the “cloud” of ions which are widely distributed in phase space. It consists out of multiple neighbouring cylindrical rings, each with an RF voltage having a phase-shift of  $180^\circ$  w.r.t. its neighbour. As the ions move through the funnel, the ions not precisely in the center move toward the plate with an opposite RF potential (compared to the ion charge). When the same plate then changes polarity, the ion will feel a stronger force towards the center of the funnel due to the higher proximity to the plate. In the center of the funnel, the RF voltages cancel out. This way the confined radially. Further into the funnel, the plates are closer to the centerline, compressing the ions spatially. Neutral air molecules hitting the ions make it so that only ions with higher velocities do not get halted, thus phase space compressing. A gradient in axial voltage over the plates drives the ions toward the octopole [48]. The ion funnel is depicted in figure 19

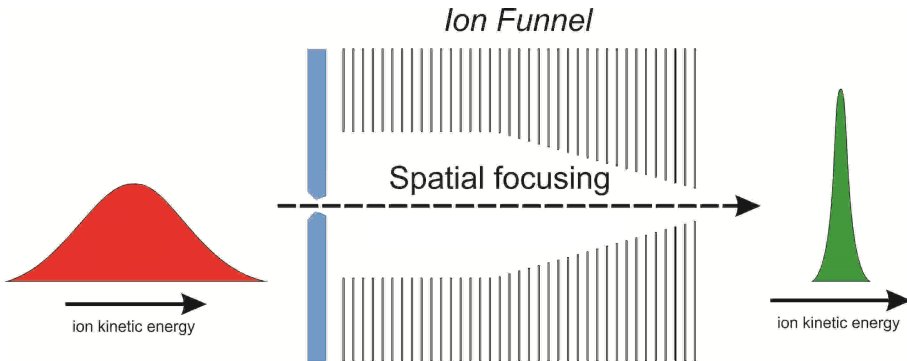


Figure 19: The basic structure of the ion funnel. Energy focusing happens due to air molecules hitting the ions.

The octopole also acts as an ion guide but primarily as an ion storage. The potential of the diaphragm in the octopole can be raised/lowered to block/transmit ions respectively, see figure 20. If the diaphragm at the entrance has the same electric potential as the diaphragm at the end, the ions will bounce back and forth. This way, a controlled pulse of ions can be let through which allows for an avoidance of the space charge problem (mentioned in 5.4) and a denser burst of ions.

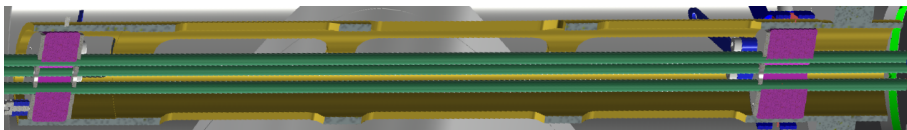


Figure 20: A technical drawing of the octopole, here the ion mirrors are on the inside of the purple PEEK insulators.

Once the ions have passed through the “gate”, they are in the mass filter. In its essence, this mass filter consists out of four rods, hence named quadrupole, positioned in a square-like geometry with each rod at a corner. Initially, the ions enter the center of this square. Only ions with a certain  $m/z$  make it through the mass filter. This can be chosen by changing the magnitude of the RF amplitude, the DC voltage applied parallel over the mass filter and the frequency of the applied field. The orbit of the ions within the trap represent Lissajous-like figures and the motion can be approximated by Mathieu’s equation:

$$\frac{d^2u}{\varepsilon^2} + (a_u - 2q_u \cos 2\varepsilon)u = 0 \quad (16)$$

Here  $u$  represents the coordinates  $r$  and  $z$ ;  $r$  being the distance to the cap on the horizontal axis and  $z$  the distance to the cap on the vertical axis.  $\varepsilon = \Omega t/2$  with  $\Omega$  is the frequency of the RF applied

to the ring.  $a$  and  $q$  are dimensionless trapping parameters and shown below for a quadrupole [49].

$$a_r = \frac{4eU}{mr_0^2\Omega^2} \quad q_r = \frac{-2eV}{mr_0^2\Omega^2} \quad a_z = \frac{-8eU}{mr_0^2\Omega^2} \quad q_z = \frac{4eV}{mr_0^2\Omega^2} \quad (17)$$

Here  $U$  is the DC potential and  $V$  the amplitude of the RF ( $V\cos\Omega t$ ) The quadrupole can act as an ion guide or a mass filter. For a low DC voltage it acts as a guide and a large selection of  $m/z$  ions can go through. The filter can be engaged by increasing the voltages until only part of the ions lie within the stability region as in figure 21. Equation 17 shows that  $a$  and  $q$  are proportional to  $\frac{1}{\Omega^2}$ , and consequently you can go up the stability region by lowering the frequency and vice versa.

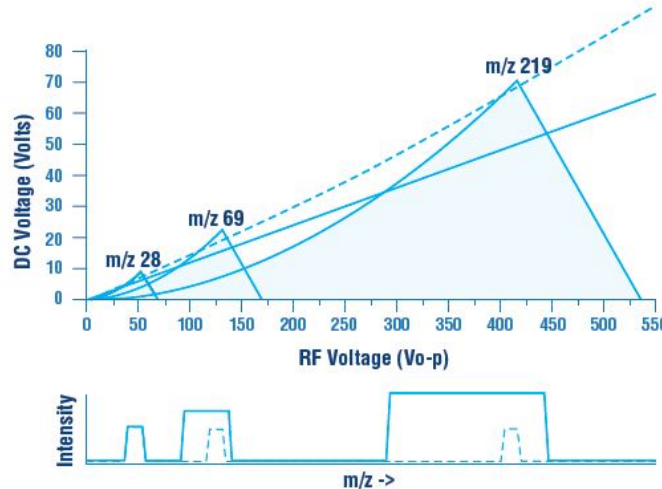


Figure 21: The Mathieu stability regions, for different masses. The dashed line represents the mass selection above which all ions are detected. If they fall out of the mountain-like peak, the stability region, they will not be detected. Source: [50].

The next stage is the Paul ion trap. The molecular beam, which consists out of particles with a certain mass, enters this compartment through a hole. Once inside, it is confined by a ring electrode through an RF field which creates a three dimensional well. You can compare this to a ball on a horse saddle, with the saddle ever spinning. Inside the trap, helium gas is let in to act as a damping agent, taking away kinetic energy and allowing entrainment. Otherwise the particles would have a too high velocity and fly through the Paul trap. The entire point of the Paul trap is, indeed, to trap ions in order to allow an interaction with other atoms/molecules. In our case atomic hydrogen. Once the interaction time is deemed enough, the RF is turned off and a waiting period on the order of a  $\mu s$  follows to make sure the ions do not get ejected from the trap while still being affected by the RF. Next, a DC voltage is applied to extract the particle out of the Paul trap.

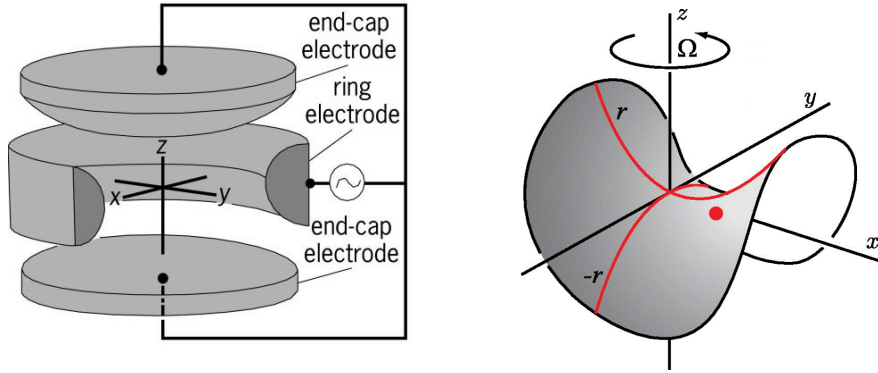


Figure 22: The operation of the Paul trap. Similar to a “saddle trap” the molecule is held in the lowest position of the potential well. Source: [51].

Not only the molecules need to enter the Paul trap, we also like to find out the reaction with e.g. hydrogen as is our goal. The hydrogen flow starts from a bottle of molecular hydrogen gas and flows through a stage consisting out of several Swagelok connections and a flow controller. This stage contains two valves to direct the flow: one to open the path for the flow which exits into the Slevin-type discharge apparatus, to be discussed, and another to allow for a larger and easier venting of the Swagelok tubing thanks to it being in direct contact with the vacuum chamber, i.e. a bypass, without any further small diameter orifices.

The flow controller is of the brand and type Bronkhorst FG-200CV and was used to fix the flow rate of molecular hydrogen going into the Slevin apparatus. A small plunger can be lifted using a magnetic force to regulate this flow rate. This magnetic force is generated by sending a PWM (Pulse Width Modulated) signal to the coil of the valve with a maximum current of 200mA. This current can be regulated and is given in “%” in the control software. To limit heat generation, the upper limit is set to 61%,  $\approx 3\text{mln/min}$ <sup>6</sup> at which the maximum flow rate has long been already been reached. This maximum flow rate of 100%, 5mln/min, will be reached for a valve output of  $\approx 35\%$ . The change in the valve output over the course of increasing the flow rate % is extremely small and depends on the flow controller valve orifice (the FG-200CV has the smallest Bronkhorst offers, at  $0.05\mu\text{m}$ ). Thus, a small change in valve output % already has a significant impact on the flow rate output. If the desired flow rate has not been reached, but the valve output is at the maximum of 61%, then there is not a sufficient supply (bottle/container is empty) or the pressure at the outlet is too high. If both are in order, the valve itself is likely to be the problem. The above is summarized in table 3.

Flow rate (mln/min)	Valve output (%)	Status
0	0	Off
5	35	Normal
5	40-45	Pressure difference is becoming critical
5	50-61	Pressure difference is critical. Check pressures on both sides. If flow rate is not attained and pressures are in order, the valve is damaged.

Table 3: Output status for the FG-200CV.

The flow of H<sub>2</sub> going into the system must not be too high as the mass detector cannot handle the subsequent higher pressure. A flow of 0.25mln/min was deemed to be enough to show hydro-

<sup>6</sup>The n stands for normal and means a recalculated flow rate for 0°C and 1 atmosphere to maintain a standard for measuring.

genation. Later, this was changed to 0.5mln/min as then the cororene should get hydrogenated more and hence a temperature dependence should be more visible. This stage is shown in figure 23.



Figure 23: The flow controller, including the connection for a bottle of inlet gas on the left. The stage can be connected to the Slevin-type discharge apparatus in the back.

After exiting the Swagelok-stage, the molecular hydrogen enters the Slevin discharge apparatus through a glass tube. The H<sub>2</sub> is exposed to radio-frequency waves at 23.6MHz and effuses as H on the bottom of the Slevin through a Teflon tube. H<sub>2</sub> alone does not dissociate by this alone, a medium needs a dipole moment to resonate with an electric field. Instead, there are electrons which resonate with the electric field. These electrons come from cosmic rays which themselves may originate from stars, but this is still disputed [52]. Now, these electrons are accelerated by the applied  $E$  field and after an avalanche of collisions with the molecular hydrogen, the H<sub>2</sub> is mostly dissociated into H and a plasma is created. This device can therefore *not* be used in a totally isolated environment, one shielded from cosmic rays, but the question is then if such an environment exists. The plasma generated has a characteristic violet hue. This hue can be ascribed to the electron transition of the hydrogen atom, from the 6th energy state to the 2nd (more specifically the principal quantum number). However, when one holds a prism in front of the eyes, the purple splits up into a red and aqua/blue color. These are the transitions from  $n = 3$  to  $n = 2$  and from  $n = 4$  to  $n = 2$ , respectively. The transitions of the hydrogen atom from a higher level to the 2nd energy level are called the Balmer series and were discovered by Johann Balmer in 1885 [53]. This is shown in figure 24.

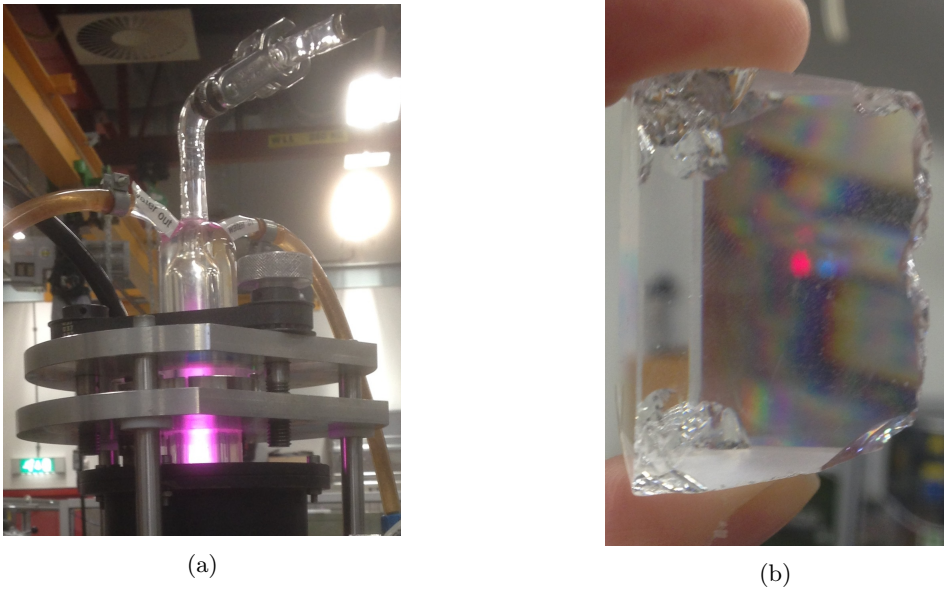


Figure 24: (a) The plasma inside the Slevin-type discharge apparatus. (b) The two Balmer-series transitions.

The power absorbed is given by equation 18.

$$\frac{P_{abs}}{V} = \frac{1}{2} n_e \frac{e^2}{m_e v} \frac{v^2}{v^2 + (f \cdot 2\pi)^2} E_0^2 \quad (18)$$

here  $n_e$  is the electron density,  $v$  the electron neutral collision rate and  $f$  the frequency of the applied field with amplitude  $E_0$  [54]. Hence, by tweaking  $E_0$  and  $f$ , one can increase  $P_{abs}$ . By increasing the frequency, one “stops” accelerating the ions, decreasing their kinetic energy. Cooling water in the adjacent compartments partly cancels the heat gained by the RF-waves. Proven effectively for many years, this set-up can reach a dissociation of up to 95% [47].

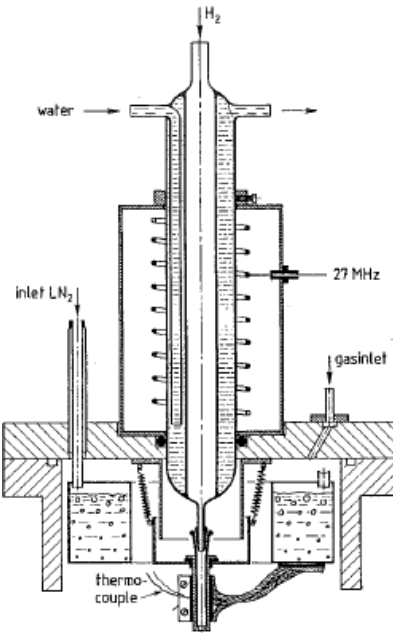


Figure 25: The Slevin-type discharge. Adapted from: [55].

The next stage is the reflectron, the specimen to be investigated enters this after leaving the Paul trap. The reflectron is a long cylindrical tube with several diaphragms at the end at a high potential. The ions traverse the length of this tube, the field free drift region and the different  $m/z$  ions take a different amount of time to traverse this length. Ions with a higher  $m/z$  have more kinetic energy and will do so in a shorter amount of time. This causes a separation in arrival times at the detector, giving a time of flight spectrum. Additionally, at the end of the field free drift region there is an ion mirror. Ions with a higher initial kinetic energy penetrate deeper inside this mirror and the time to turn around is bigger than for ions with lower initial kinetic energies. The result is that this spread in initial energies is negated if the mass detector at the end of the flight path is placed at the correct position such that different energetic ions (with the same mass) arrive at the same time. The process is illustrated in figure 26.

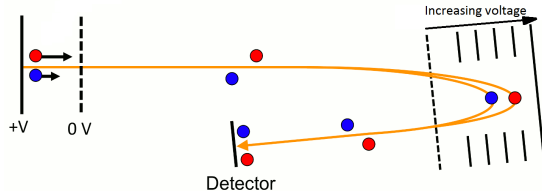


Figure 26: The higher energy ion (blue) takes a longer path but arrived at the same time as the lower energy ion (blue). Adapted from: [56]

The  $m/z$  value of the ions can be approximated from the time of flight value by using equation 19 [57]:

$$\frac{m}{z} = 2eEs\left(\frac{t}{d}\right)^2 \quad (19)$$

where  $s$  the distance between source and extraction,  $z$  the charge and  $E$  the electric field that accelerates the particles in field free drift region  $d$ . However, this equation does not take into

account the reflectron region and is only valid for a “simple” linear mass spectrometer. From this the resolution of the measuring apparatus can be determined i.e. the ability to separate ions of similar flight times into separate signals. Often, the resolution of the full device is denoted as  $m/\Delta m$  where  $\Delta m$  is the peak width of the signal. This is also often denoted as  $Q = \frac{w_0}{\gamma}$  in atomic physics where  $w_0$  is the frequency and  $\gamma$  the line width at FWHM. In the case of separation two ions with masses 300 and 301, the resolution only needs to be  $300/1 = 300$  and increases for higher masses. The mass detector itself consists out of several microchannel plates which creates an avalanche of electrons after being hit. Each hit thus creates an electrical pulse which is sent to a digitizer to measure the pulse arrival time, shape and amplitude.

### 3.2 The BalUn

The mass filter or the quadrupole, which regulates which masses move into the stability region of the Mathieu equations, is regulated by a BalUn. The BalUn receives an (unbalanced) RF frequency and splits it up into two (balanced) frequencies which have a phase difference of  $180^\circ$  w.r.t. to each other. BalUn is a portmanteau for balanced and unbalanced. Unbalanced means that the current is working against ground (like in a coax cable) so that all the energy moves through the center while balanced means the current in the two signals are working against each other i.e. the voltage of one output is opposite the other. The *need* of this is because, taking the coax cable as an example, in an unbalanced system the central conductor will radiate EM fields outward unless the shield is grounded. The balanced part will not radiate anything outward. Unfortunately, feeding a two balanced signals right into a dipole (or quadrupole in our case) would not work because the two signals coming from two separate amplifiers do not have a constant phase difference at all times. An unbalanced and balanced system example is shown below in figure 27.

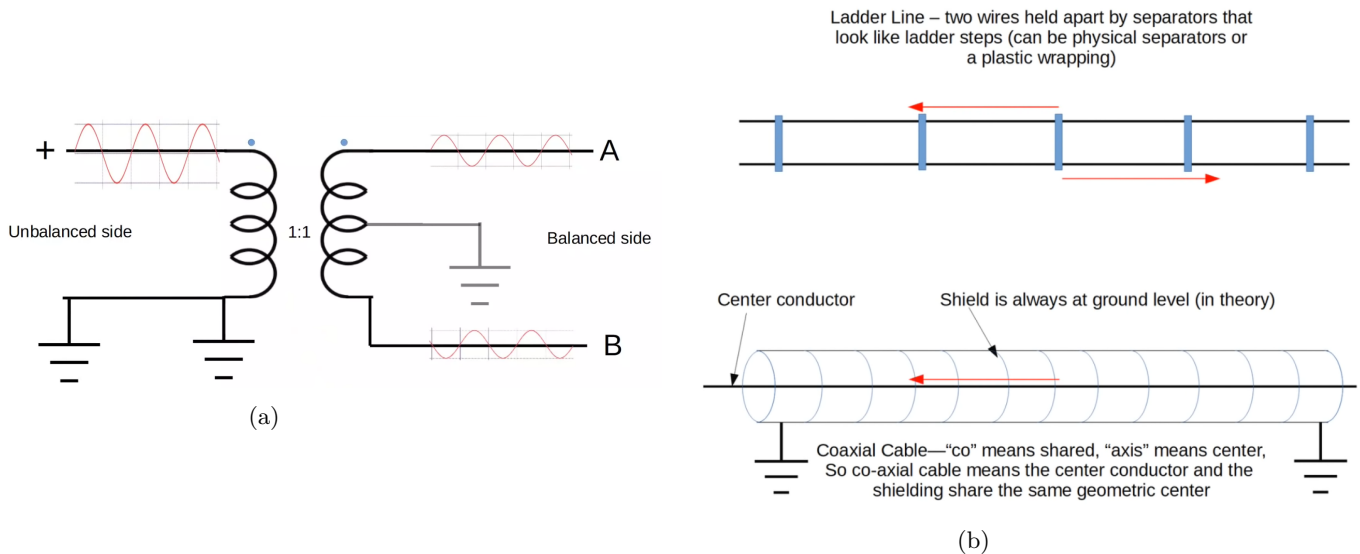


Figure 27: The BalUn. (a) a schematic of how a 1:1 BalUn transformer splits up a signal from unbalanced to balanced. (b) Here the red arrow represents the current which switches direction over time (AC). On the top a balanced ladder line system and on the bottom a coax cable which is unbalanced. Adapted from: [58].

In the course of our experiments, as will be explained, the signal generator for the quadrupole broke down. The signal generator is commercialized as a mass filter and made sure that a proper balanced signal arrived at the quadrupole to filter out masses.

## 4 Design

### 4.1 Teflon tube encasing

The dissociated hydrogen is cooled by the liquid nitrogen bath at the bottom of the Slevin apparatus. A copper block allows for thermalization between the Teflon acting as a transport tube for the hydrogen and the liquid nitrogen bath inside the Slevin apparatus. The inner diameter of this tube is 3.2mm and the outer diameter is 7mm. Teflon was chosen because it has a very low sticking coefficient ( $\approx 0.05$ ) [59] and because it is an electric insulator (to make sure any stray fields within Paultje are not affecting the flow) which also prevents any electric field building between the Paul trap and the Teflon such that the RF in the Paul trap is not affected. The copper and the Paul trap might form such a capacitor like system but this was not tested.

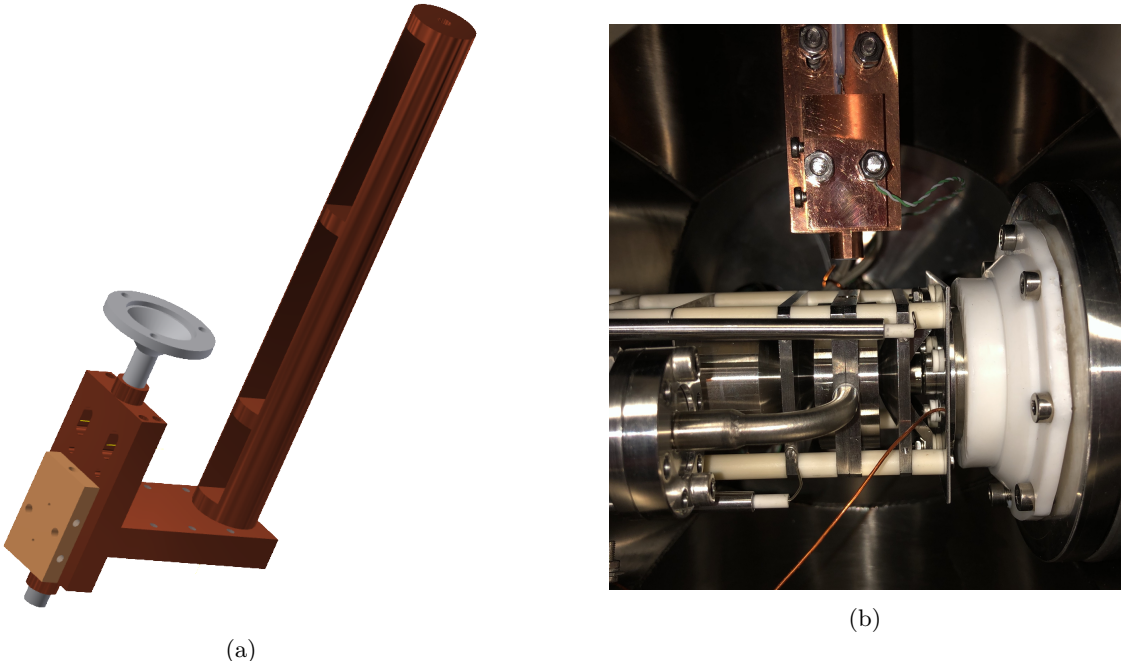


Figure 28: (a) The Teflon tube that carries the atomic hydrogen out into the Paul trap, with the copper encasing. The tube extends a bit for illustration purposes, but is fully encased in reality to avoid a temperature difference. (b) The Teflon tube + encasing mounted above the Paul trap, in order to avoid any electromagnetic coupling with the copper.

As we need the copper encasing to have no temperature gradient along its vertical axis, we put the heating elements in the central rectangular block. The atomic hydrogen exits the Teflon tube as in figure 28b and has to traverse a small distance before entering an opening to the Paul trap.

### 4.2 Thermal shrinking

As the Teflon tube shrinks more than copper when cooled down, the two might lose contact. To compensate for this, the copper encasing is put under tension with springs, tightened by nuts, to still adhere to the tube due to internal tension. This can be calculated via equation 20:

$$r_{new} = r_{old}(\Delta T \alpha + 1) \quad (20)$$

where  $\alpha$  is the heat expansion coefficient of that material and  $r$  the radius. Teflon has an expansion coefficient  $\alpha \approx 86 \cdot 10^{-6}/^\circ C$  [60] while copper has  $\alpha \approx 15 \cdot 10^{-6}/^\circ C$  in the range 100K-293K. For

two cylinders with  $r = 0.0035m$ , representing face-to-face contact, and cooling from 293K to 100K, the difference in diameter is 0.0479605mm. This difference is small enough to be compensated by tightening.

### 4.3 Heat flow of the encasing

We can model the heat flow through the copper encasing using COMSOL. As Teflon is a poor thermal conductor, as are all plastics due their covalent bonding nature, we need to check whether the point where the temperature is measured via sensors and the inner part of the Teflon tube do not deviate too much. This was also simulated in COMSOL and showed a temperature difference of no more than 3 degrees. A first design had the Teflon tube stick out of the copper encasing at the bottom but this would give a deviation of 15 degrees.

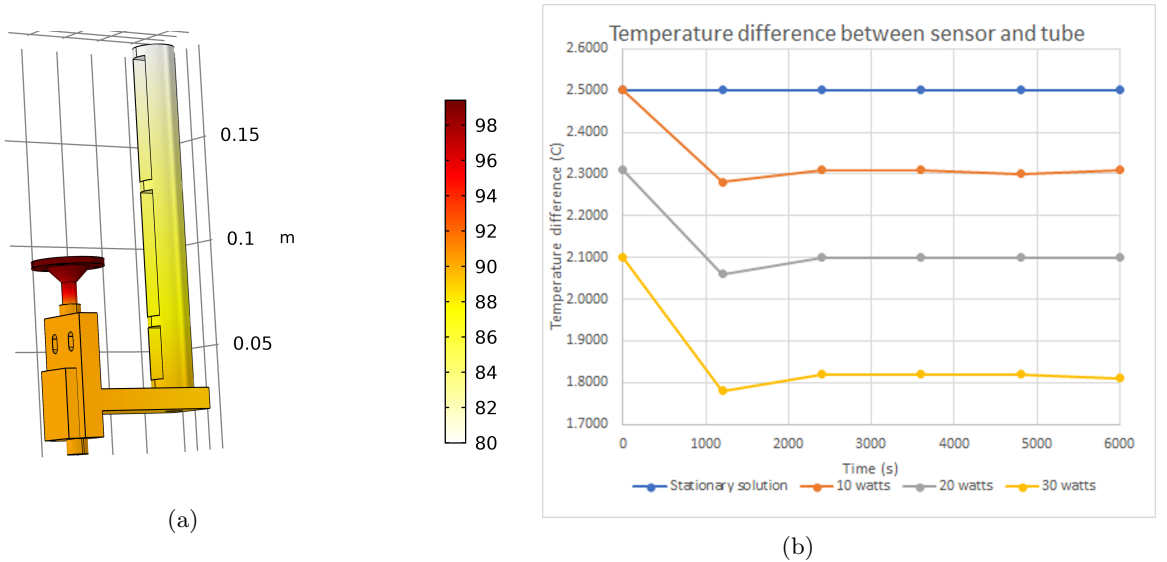


Figure 29: (a) Heat conduction simulation, no heating and N<sub>2</sub>(l) cooling for 10 minutes followed by an incremental 10W increase in heating for 6000 seconds. (b) Difference in temperature between sensor position and inner tube for various wattages. The blue line shows the final temperature deviation for 0 watts.

Grey-body radiation inside Paultje  $\approx 293W/m^2$  at room temperature (20°C conditions, which causes the temperature of the copper to be unable to reach liquid nitrogen temperature. This number can be calculated using the Stefan-Boltzmann law, for stainless steel with an emissivity of 0.7.

$$P = \epsilon\sigma AT^4 \quad (21)$$

Here  $\epsilon$  is the emissivity of the material,  $\sigma$  the Stefan-Boltzmann Constant,  $A$  the surface area and  $T$  the temperature.

In case the contact between the Teflon and copper encasing is not firm, the cooling would only be done by radiation which, if a separation distance of 1mm exists, would only cool down the tube by 1 degree after 10 minutes, also simulated.

### 4.4 PID heat controller

The PID controller controls the temperature with two nickel-chromium heating elements, in parallel each rod with a maximum power output of 100W, of the brand and type Firerod C2A5 and a

temperature sensor. The temperature sensor is a PT100 Resistance Temperature Detector (RTD) which has a steady linearity for low temperatures down to -200°C. The PT100 is a wire-wound ceramic sensor that is made by winding a platinum wire into a coil. The coil itself lies within a ceramic body and is surrounded by alumina powder to avoid any short-circuiting and offer robustness. There is no air inside the ceramic body. Once the Teflon tube has reached the lowest temperature (80-100K), the PID controller will calculate the PID values to accurately increase the temperature in small steps. The PID controller sends a small current through the PT100 after which the voltage drop over it is measured, then using Ohm's law the resistance can be calculated. As the PID controller cannot use a K-thermocouple as a feedback mechanism to such low temperatures, this was the only viable option. An extra K-thermocouple was installed however, to make sure that the PT100 read the correct temperature. This was not the case. The error could be attributed to an unequal heat contact with the copper block or due to the feedthrough that has wiring made from aluminum and chromel instead of copper. A three or four wire sensing RTD could solve this. Nevertheless, by coupling the "true" thermocouple temperature to the PT100 temperature we can get rid of this ill measurement, see figure 30a.

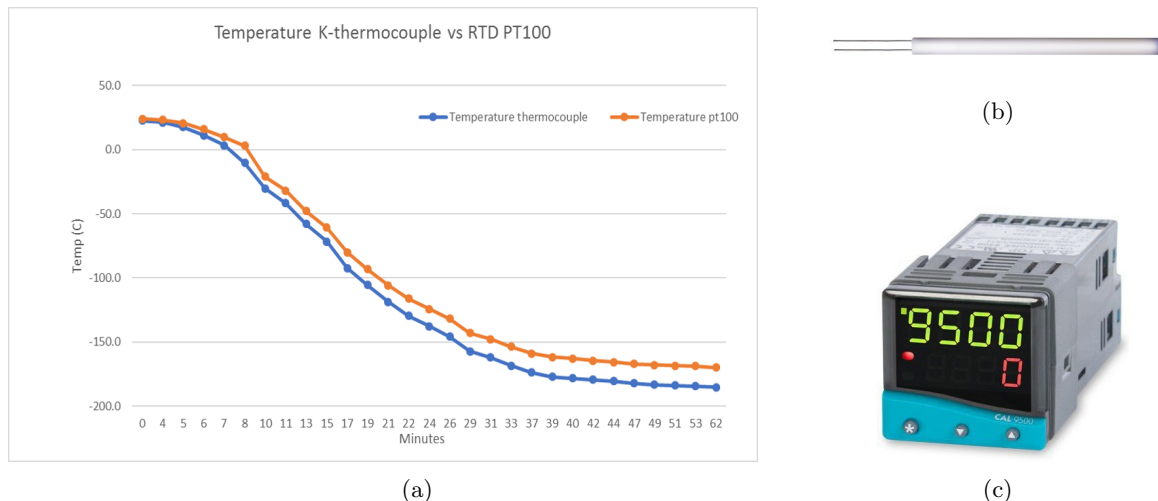


Figure 30: (a) The discrepancy between the PT100 and the thermocouple (b) The PT100 sensor (c) The PID device, CAL 9500P.

To make sure the thermocouple temperature is correct, one can make a reference measurement. This is done by connecting one end of the thermocouple wires to something you want to measure (say a block at 30°C) and the other to an ice bath at constant temperature. At 0°C, all thermocouples do not measure potential difference as it is engineered that the Fermi levels of both materials are aligned for this  $\frac{\text{material1}}{\text{material2}}$  ratio. Now one can make a table and compare the voltages and voltage change per degree; the Seebeck coefficient. If they do not match, one can set up a different Seebeck coefficient to match the temperature range. This problem was avoided by us as we used a designated K-thermocouple measurement device.

## 5 Experimental results of attaching hydrogen and deuterium to PAHs

### 5.1 Hydrogenation of cororene

In order to find out if the cororene + H has been affected by the temperature, we take the mass spectrum and compare it for different temperatures. As the hydrogen atoms at higher temperature will have a higher energy, it is expected that there will be more hydrogenation than for lower temperatures due to the overcoming of the energy barrier. The cororene and the incoming H were allowed to remain in the trap for 3 seconds before extracting them towards the mass detector. Firstly, a spectrum was taken at room temperature to act as a reference point, after which the copper + Teflon were cooled down to -166°C. Subsequently, data was taken for equidistant intervals up to +105°C. As every measurement requires a thermalization period of about 10 minutes, this was the period we had to wait before taking acquisitions. Only for the first spectra in figure 31 there were no reference temperature recorded but in further measurements there is. There are two ways to plot the data; either plot the peak heights with an error bar equal to  $\approx \frac{FWHM}{2.355}$  or the integral of the peak. The latter was chosen as it is for a clearer normalization representation on the y-axis and one can better compare the experimental to the theoretical results.

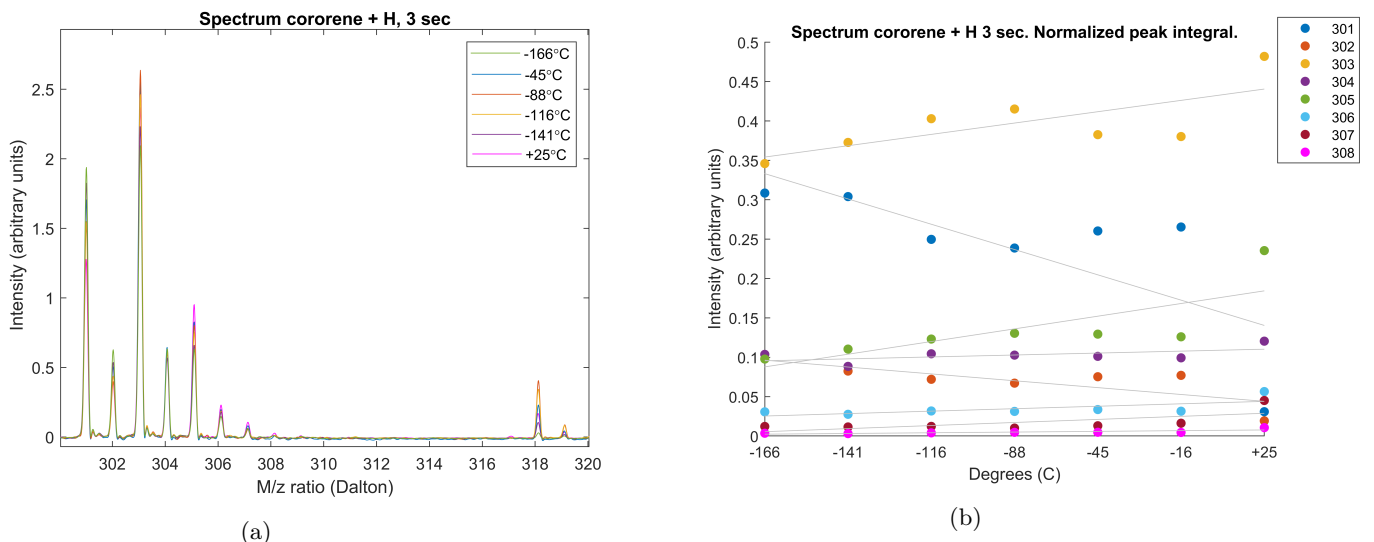


Figure 31: (a) The m/z spectrum for different temperatures for a flow of 0.25ml/min. (b) The normalized peak integrals for various masses at different temperatures.

At first glance it is obvious that the peak heights alternate between a high and a lower peak. This is because the energy barrier for odd numbers is lower than for even numbers and can be explained by the fact that the odd numbers are “open-shell” and the even numbers are “closed-shell”, meaning the sum of spin ups and down is different and the same, respectively. There is a slight peak at  $m/z = 318$  which could be attributed to  $H_2O$  or  $CH_3$  which stick to the precursor cororene and previously hydrogenated cororene (that is, the 303) respectively. As this peak should have been filtered out by the mass filter, this leaked in after that part of Paultje. This was discovered and fixed after and including figure 35. In figure 31, 50 acquisitions were taken for each temperature and the flow of molecular hydrogen exiting the flow controller was set to 0.25ml/min. After this initial experiment, we changed the flow to 0.5ml/min to see if the temperature effect is more prominent as depicted in figure 32a. The number of acquisitions remained 50. In figure 32b, the position of the peaks is given for the different temperature measurements.

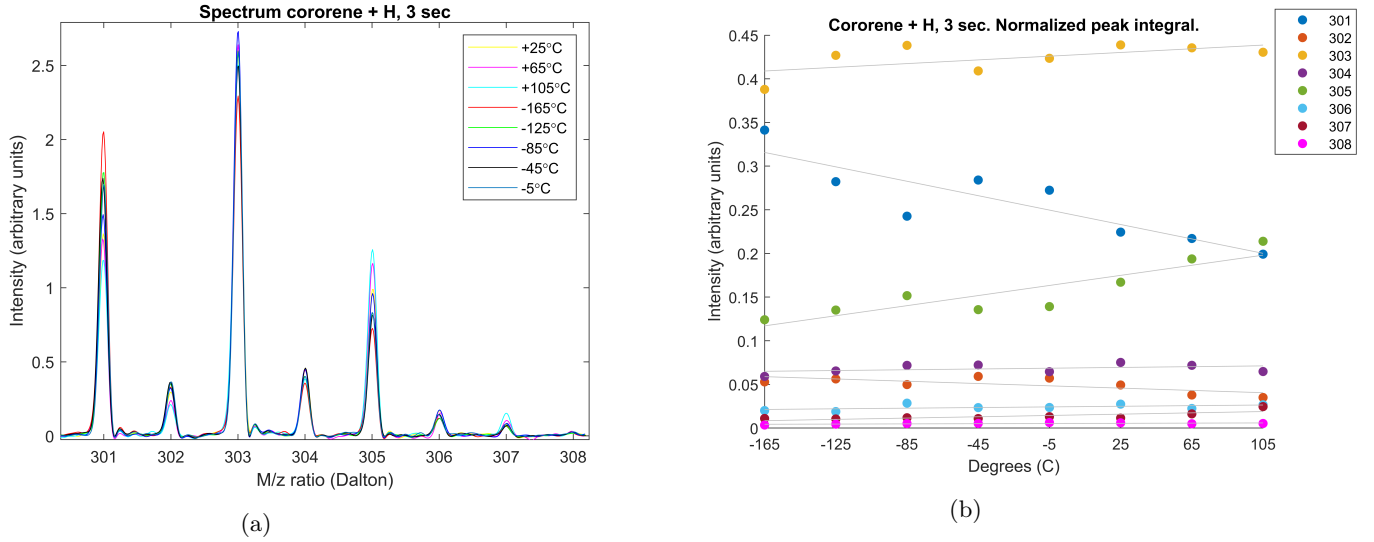


Figure 32: (a) The  $m/z$  spectrum for different temperatures for a flow of 0.5ml/min. (b) The normalized peak integrals for various masses at different temperatures.

The  $305\text{ }m/z$  peak increases with temperature which hints at that the atomic hydrogen has indeed gained more energy from the heated Teflon tubing and is able to further hydrogenate the cororene. The  $303\text{ }m/z$  increases slightly and the  $301$  and  $302$  actually decrease. This further reinforces the cascading flow on how the hydrogenation takes place. The cascading flow method is explained in section 5.3. Of course, we have to check if the spectrum before any change in temperature is the same after the cooling down to the lowest temperature and then heating up again. This was done for the same settings of Paultje and the same sample composition:

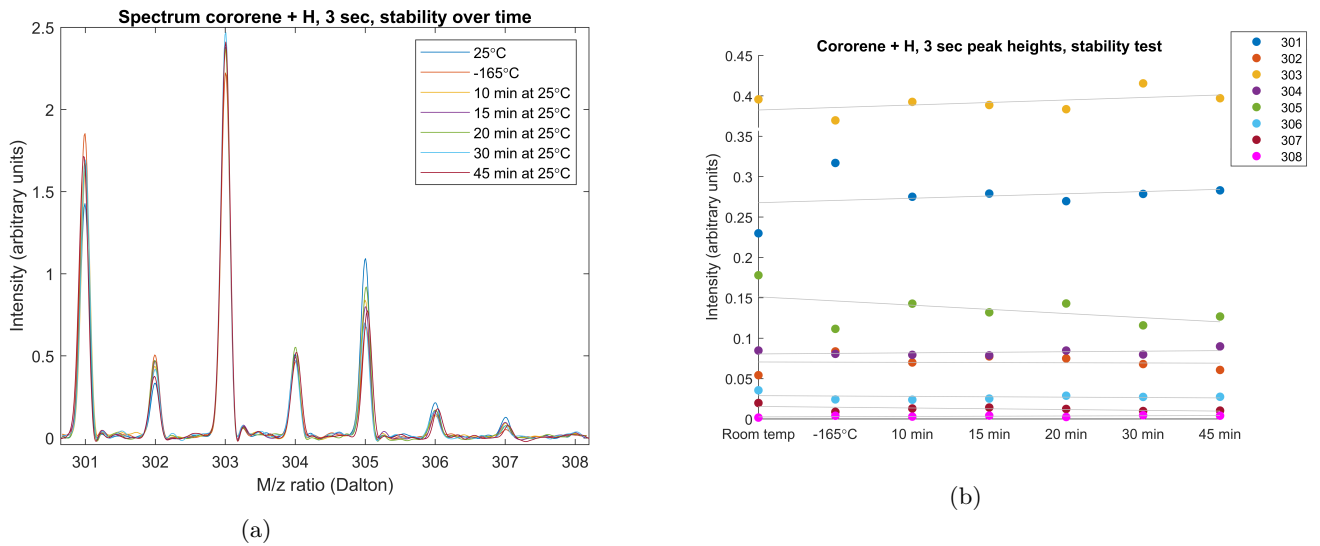


Figure 33: (a) The  $m/z$  spectrum for different temperatures for a flow of 0.5ml/min. (b) The normalized peak integrals for room temperature ( $25^\circ\text{C}$ ), the lowest temperature, and then after heating up back to room temperature with a certain waiting time after attaining this.

As can be seen from figure 33, the spectra before and after the temperature change are not the

same, although the difference is small. There could still be some H atoms frozen to the inside of the Teflon tube which take longer than an hour to get rid of. As mentioned before, there was also a leak into the system but besides that the mass filter stopped working. The result of these two mistakes is shown below for when cororene and the atomic hydrogen interacted in the Paul trap for 1 second before extraction. The amount of acquisitions was 250.

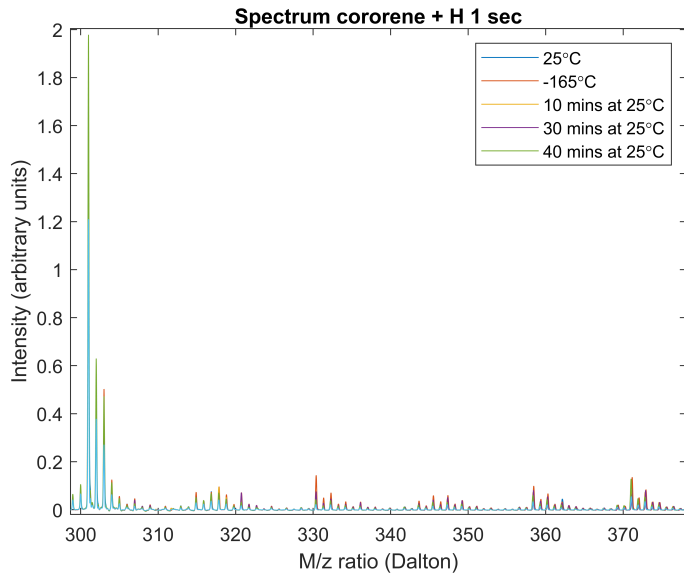


Figure 34: The m/z spectrum which shows contamination after the initial hydrogenation.

After the above experiment, the mass filter stopped working entirely so we installed our own. This is explained in section 3.2. Once the BalUn replacement was into place, more measurements were taken to see if we can get back the temperature dependence like in figure 32. We also found a leak in the Swagelok stage that is now closed which showed up as contamination in all results before, depicted in figure 31a. The result is shown below.

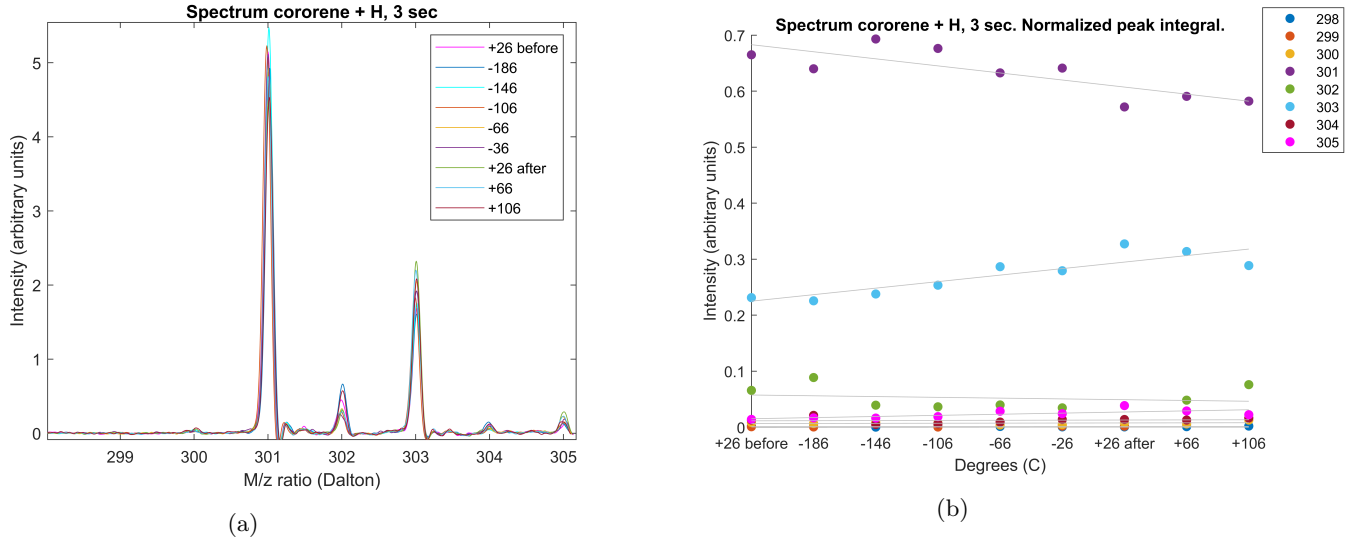


Figure 35: The spectra after the BalUn device was installed. (a) The  $m/z$  spectrum for different temperatures. (b) The peak integrals for various masses at different temperatures.

It is clear that the hydrogenation is much less than in previous experiments despite using the same flow rate. Either the Teflon tube is damaged or the several sections that comprise the Teflon tube are not well connected. On the other hand, the BalUn replacement works better than the previous commercial mass filter as the spectrum is much cleaner. There is a temperature effect but the bulk of the molecules now have a  $303\text{ }m/z$ . This indicates the temperature effect is less pronounced than in figure 32b.

## 5.2 Deuteriation of cororene

Below, the spectrum for the deuteration of cororene is plotted. What is striking is the further attachment of atoms/molecules to cororene at a  $m/z$  of 320 up till and including 325. As we saw something similar in the hydrogenation spectrum in figure 31a, the obvious conclusion one can make is that it is still something similar like  $\text{H}_2\text{O}$ . However, this would then show as a peak at 318 too. The peak, in the scenario of  $\text{H}_2\text{O}$  addition, at 320 is too small compared to the peak 321 if one compares this to the 300 to 301 peak ratio. These contaminations also decrease once the temperature cycle begins and nearly disappear for  $+106^\circ\text{C}$ . This time it was chosen to not plot the peak integral, but the peak intensity to showcase the error for 100 acquisitions that were taken.

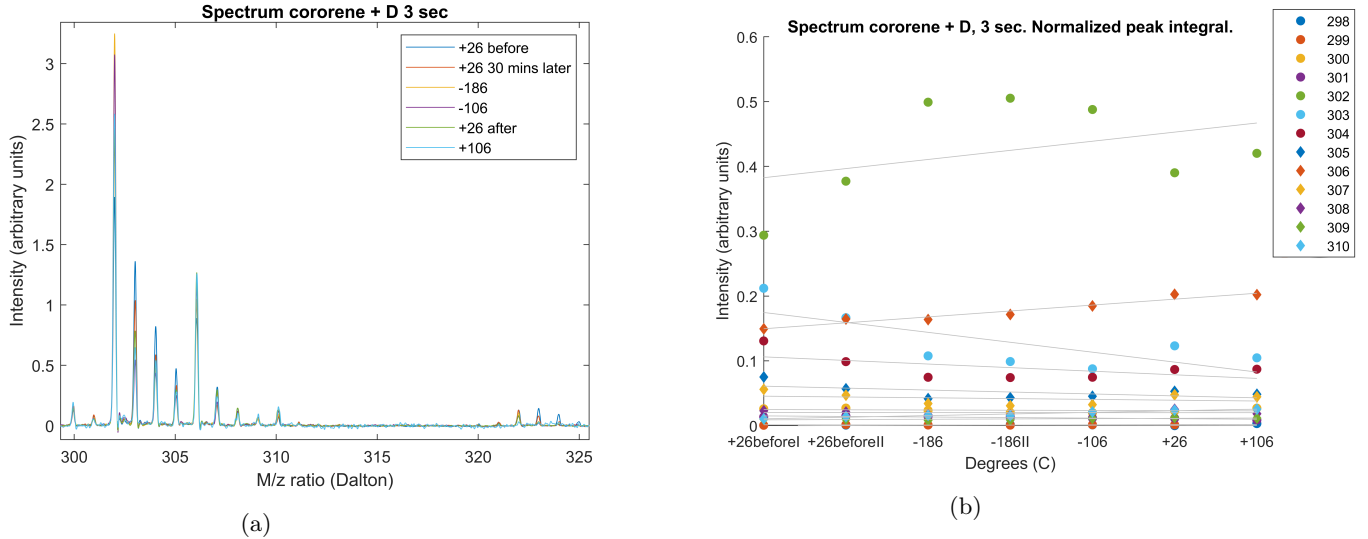


Figure 36: (a) The  $m/z$  spectrum for different temperatures. (b) The peak heights for various masses at different temperatures.

The results in figure 36b show primarily that the  $303\text{ }m/z$  decreases and the  $306\text{ }m/z$  increases, again showing a temperature effect. However, the  $302\text{ }m/z$  also increases slightly. This is because the masses change by 2, as opposed to 1 in the hydrogen case. The  $303\text{ }m/z$  comes from an addition of deuterium to the  $301\text{ }m/z$  and decreases as the temperature increases. The  $+26\text{degrees I}$  and  $+26\text{degrees II}$  were measured with a short pause in between because the signal got too weak.

After further investigation of the tubing, because no temperature effects were noticeable anymore, it appeared that the Teflon tube moved downward about 1mm. This indicates bad contact with the encasing so we had to refit it into the copper casing even more firmly. Also, dark fringes appeared on the inside of the Teflon tube, in a periodic fashion (about 2mm apart). This is further discussed in section 6.1.

### 5.3 Cascading flow

All peak integral figures show a trend. That is, a cascading flow is shown when going from lower to higher temperatures. This is illustrated in figure 37

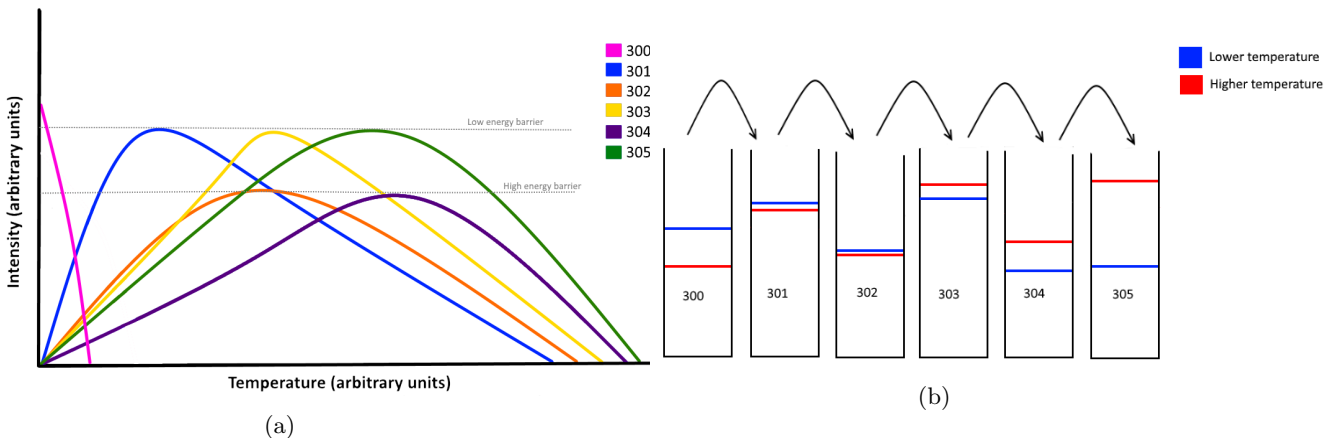


Figure 37: (a) Sketch on how the distribution varies with temperature (b) Order of occupying the various  $m/z$  for a lower and higher temperature

At lower temperatures, the lower  $m/z$  fill up after which an additional hydrogen atom may stick to this  $m/z$  to increase the mass by 1. The next addition may only happen once there is at least one  $m/z + n$ , where  $n$  is the amount of additions. The intensity is capped off by the dotted grey lines as then the full hydrogenation is reached for that  $m/z$ . For the  $m/z$  with a high energy barrier (that is the even amount of  $m/z$ ), the intensity is not as high as the odd  $m/z$  because these molecules quickly gain one hydrogen atom due to the following lower barrier. This kind of pattern continues unless the energy barrier changes from the regular low/high pattern. The solid blue and red lines in the right figure represent the amount of hydrogen atoms attached, the higher the line, the higher the amount. An ensemble of hydrogen atoms having a higher temperature, individually having more kinetic energy, will hydrogenate the cororene more because the probability to overcomes the energy barrier becomes higher. This shifts the main contribution  $m/z$  more to higher end. Hence, the bulk of  $m/z$  will have a higher number for a higher temperature, which is evident from most figures in the previous subsections. What follows now is to go through each figure and see which  $m/z$  grows at the expense of other lower  $m/z$ .

In figure 31b, the 303 and higher all increase in intensity while the 301, 302 drop. The higher  $m/z$  ratios ( $> 305$ ) do not increase as much as the temperature is not high enough to have the main contribution be concentrated here. As the last data points at +25C are outliers it is better to look at figure 32b.

As mentioned before, figure 32b shows an increase in any  $m/z$  above and including 303 while the 301 and 302 drop. The 303  $m/z$  does not decrease, even for higher temperatures like 105C. This indicates that it has not been saturated yet to allow for a big increase in the masses higher than 303; those only increase slightly. The rise in the 305  $m/z$  indicates a the total distribution indeed shifts more to higher  $m/z$  for higher temperatures.

The last hydrogenation plot, figure 35b, again shows a decrease of the lower  $m/z$  ratios (a high gradient decrease for the 301) and an increase in  $m/z$  ratios for cororene with a mass of 303 and higher. However, here the main concentration of the mass distribution is located in the 303  $m/z$ , instead of the 305 as in figure 32b. This could be because the temperature is not high enough to let the "cascading flow growth" concentrate in the 305 peak due to technical problems mentioned before.

In the deuteration plot, figure 36b, a slightly different trend appears. The 302  $m/z$ , the first

addition, keeps on growing which at first indicates the temperature effect does not let the main contribution "flow" to higher  $m/z$ . However, the 303, 304 and 305  $m/z$  all decrease while the 306  $m/z$  increases, proving the contrary. This could be attributed to abstraction mechanisms, hinting at a complicated network of  $m/z$  flow. Two possible mechanisms are:  $\text{C}_{24}\text{H}_{12}\text{D}_s + \text{D} \longrightarrow \text{C}_{24}\text{H}_{12}\text{D}_{s-1} + \text{D}_2$  which has a loss of 2  $m/z$  or  $\text{C}_{24}\text{H}_{12}\text{D}_s + \text{D} \longrightarrow \text{C}_{24}\text{H}_{11}\text{D}_s + \text{HD}$  with a loss of 1  $m/z$ . If true, increasing the temperature increases this abstraction mechanism which would lead a significant part of the  $m/z$  distribution end up in the 302  $m/z$ .

To conclude; all plots show the same trend; with increasing temperature the  $m/z$  ratios move to higher numbers.

#### 5.4 Line broadening

The experimental  $m/z$  spectrum shows a line broadening. This can be attributed to both the fundamental physics and the experimental set-up. Firstly, because the packet of ions inside the Paul trap is not a singularity, the ions that are more towards the exiting hole get accelerated less. The ions that are further away get accelerated more. Over a longer distance, this will create a difference in path length which will show up in the spectrum. Secondly, the ions in the Paul trap suffer from the space charge problem; negative ions repel each other. Thirdly, the meshes at the end of the reflectron may not be entirely flat. This can cause the ions to experience a different potential which, again, causes a difference in path length.

#### 5.5 Extraction of the energy barrier

As can be seen from the experimental results, the hydrogenation and thus the peak heights at higher  $m/z$  increase for longer times and should also for higher temperatures. This change, along with equation 7, can be used to obtain the energy barriers using a Fortran script made by the group of Stephanie Cazaux. The reaction rate,  $k$ , can be computed by estimating the number of H atoms and  $\text{Cor}^+$  molecules we have in the Paul trap. For example: in the case of  $\text{Cor}^+$ :

$$\text{First order reaction : } -\frac{\Delta \text{C}_{24}\text{H}_{12}^+}{\Delta t} = k[\text{C}_{24}\text{H}_{12}^+] \int_{|\text{C}_{24}\text{H}_{12}^+|_0}^{|\text{C}_{24}\text{H}_{12}^+|_t} \frac{d[\text{C}_{24}\text{H}_{12}]}{[\text{C}_{24}\text{H}_{12}]} = \int_0^t -kdt \quad (22)$$

Once  $k$  has been obtained, we can use the model to alter the energy barrier of the sequential attachment of hydrogen. The inputs in that theoretical model that we can change are: temperature of the target molecule and the atomic beam, number density, and interaction time between molecule and atom. The chemical network (pathway of molecule formation), abstraction mechanisms, cross sections and attachment sites remain the same.

The energy barriers are obtained from DFT simulations and inserted into the script as well. These initial energy barriers are shown below in table 4 [37]. As explained before, the barrier alternates between a high and low value because of an even to odd number of electrons, paired and unpaired.

Before	Addition	After	Cross-section ( $\text{\AA}^2$ )	Energy barrier (eV)	Attachment sites	Mass before	Mass after
Corp	H	CorHp	1.1	0.01	12	300	301
CorHp	H	CorH2p	1.1	0.03	1	301	302
CorH2p	H	CorHp + H2	0.55	0.01	1	302	300
CorH2p	H	CorH3p	1.1	0.01	4	302	303
CorH3p	H	CorH2p + H2	0.55	0.01	1	303	301
CorH3p	H	CorH4p	1.1	0.03	1	303	304
CorH4p	H	CorH3p + H2	0.55	0.01	4	304	302
CorH4p	H	CorH5p	1.1	0.01	1	304	305
CorH5p	H	CorH4p + H2	0.55	0.01	5	305	303
CorH5p	H	CorH6p	1.1	0.10	4	305	306
CorH6p	H	CorH5p + H2	0.55	0.01	6	306	304
CorH6p	H	CorH7p	1.1	0.01	1	306	307
CorH7p	H	CorH6p + H2	0.55	0.01	6	307	305
CorH7p	H	CorH8p	1.1	0.10	1	307	308
CorH8p	H	CorH7p + H2	0.55	0.01	6	308	306
CorH8p	H	CorH9p	1.1	0.01	1	308	309
CorH9p	H	CorH8p + H2	0.55	0.01	6	309	307
CorH9p	H	CorH10p	1.1	0.03	1	309	310

Table 4: The different inputs to the theoretical model used to match it with the experimental data, where p stands for protonated (+) and +H2 is an abstraction.

The output of the script gives the ion yields and this theoretical data can be compared to the data obtained experimentally. By changing the the theoretical energy barriers,  $E_{act}$  can be optimized until the yields overlap with the experimental data. As a result, one obtains the energy barrier. The results are shown in figure 38:

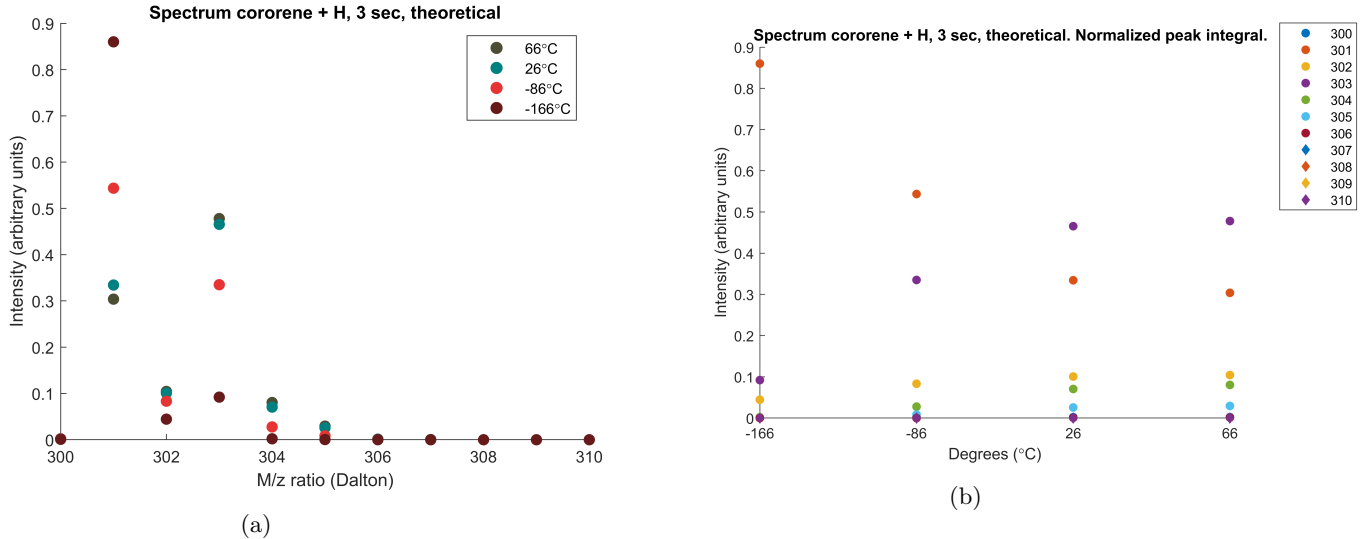


Figure 38: (a) The theoretical  $m/z$  spectrum for various temperatures. (b) The peak heights for various masses at different temperatures.

With the theoretical model, one can fit the yields onto the experimental results.

A parameter that still needs to be found is the correct initial density of the cororene ( $m/z = 300$ )

within the trap and the hydrogen beam flux. At the moment this is clearly too low since the hydrogenation already starts to drop drastically at  $m/z = 305$ , which does not happen for the experimental data. One can guess both the flux and density and see if the theoretical and experimental values overlap, after which the search for  $E_{act}$  can begin by tweaking the temperatures. For a cororene desntiy of  $10^6/cm^3$  and a hydrogen density of  $10^{10}/cm^3$  the trend looks to be reproduced but the theoretical model is a bit too sensitive to temperature. Hence we have to alter the probability for which the H atom overcomes the energy barrier of the cororene. At the moment this is similar to equation 7,  $P_b = e^{(-E_a \cdot 11604/T_h)}$  where 11604 is a conversion factor in Kelvin/eV. This stems from the probability to lie in an interval past  $E_a$ :

$$P(E, E + dE) = \frac{e^{-E/k_b T} dE}{\int_0^\infty e^{-E/k_b T} dE} = \frac{e^{E/k_b T} dE}{+k_b T}$$

$$P(E > E_a) = \int_{E_a}^\infty e^{-E/k_b T} dE = -e^{-E_a/k_b T} \quad (23)$$

This could be for 3 reasons:

1. In the theoretical model, only thermal hopping is considered. However, we should also include a quantum tunneling term. Quantum tunneling is dominant at lower temperatures as the hydrogen atom has less kinetic energy. The extra quantum tunneling term is the transmission coefficient:

$$T(L, E) = \frac{1}{\cosh^2(\beta L) + (\gamma/2)^2 \sinh^2(\beta L)}$$

$$(\gamma/2)^2 = \frac{1}{4} \left( \frac{1 - E/U_0}{E/U_0} + \frac{E/U_0}{1 - E/U_0} - 2 \right) \quad (24)$$

Here  $L$  is the potential well width  $U_0$  the energy barrier,  $E$  the energy of the incoming particle and  $\beta = \frac{2m}{\hbar^2}(U_0 - E)$  [61]. Simply using the equipartition theorem we can estimate the incoming particle's energy as  $\langle E \rangle = \frac{3}{2}k_b T$ . The width and height of the barrier are then tunable variables.

2. The sticking of H atoms decreases as T increases because they escape the potential well of the cororene. The sticking coefficient is not well mapped. The most recent study from 2012[62] suggest the following sticking coefficient - temperature dependence:

$$S(T) = S_0 \frac{1 + \beta T/T_0}{1 + T/T_0}^\beta \quad (25)$$

where the 0 denotes zero temperature;  $T_0 = \frac{2mc_0}{k_b}$ . Here  $c_0$  is the mean value of the critical velocities below which the atoms stick independent of the interaction with the molecule.  $\beta$  reflects the geometry of the incident beam. For an effusive beam this is 2.22. Most up to date values are  $S_0 = 1$  &  $T_0 = 25K$ .

3. The theoretical energy barriers are not correct.

After accounting for the sticking coefficient, it appears that the density of cororene is barely influencing the cascading flow as opposed to the flux of the hydrogen beam.

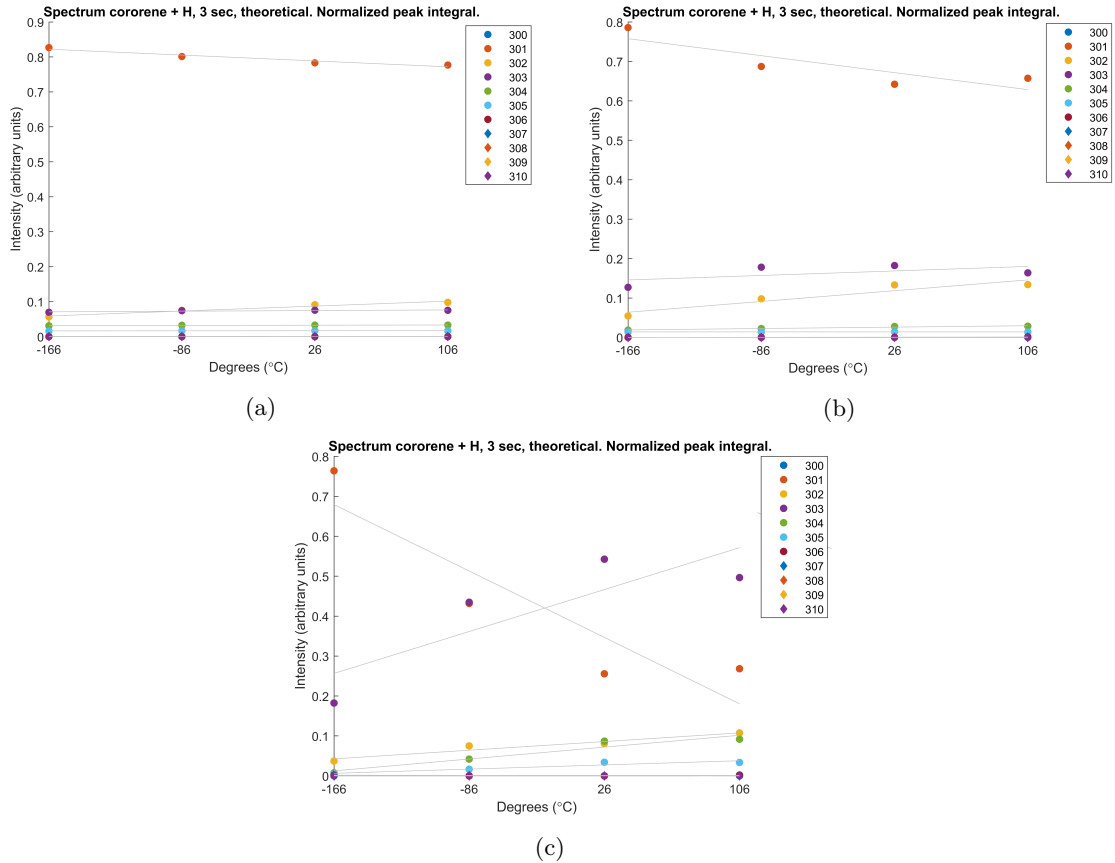


Figure 39: (a) Theoretical plot for a cororene density of  $10^6/cm^3$  and a hydrogen flux of  $10^{10}/cm^3$   
(b) Hydrogen flux of  $10^{11}/cm^3$  (c) Hydrogen flux of  $10^{12}/cm^3$

For a flux of  $10^{11}$ , the theory matches experiment the best. However, the adjusted theoretical plot 39 looks to be exponential while the experimental plot 35b is linear. The 302 line is also too high at all times. A next logical step would be to then lower the energy barrier for the transition from 302 to 303. Another idea would be to lower all 0.01eV barriers to 0.005eV:

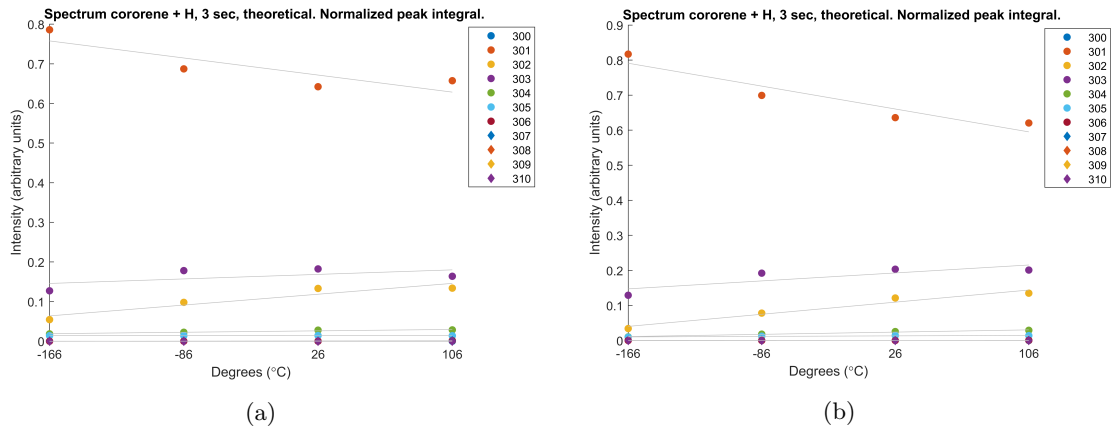


Figure 40: (a) Changing the energy barrier for the 303 m/z to 0.002eV for a cororene density of  $10^6/cm^3$  and a hydrogen flux of  $10^{11}/cm^3$  (b) Changing all 0.01eV barriers to 0.005eV

The first change has barely shows any change. The second plot shows the 301 declining too much and the 302 still appearing above 0.1. As formula 25 was modeled for a grain at 10K while our cororene is probably 300K, we are at liberty to change this equation such that it is slightly less dependent on the hydrogen's kinetic energy. Adding a simple prefactor of 25 yields:

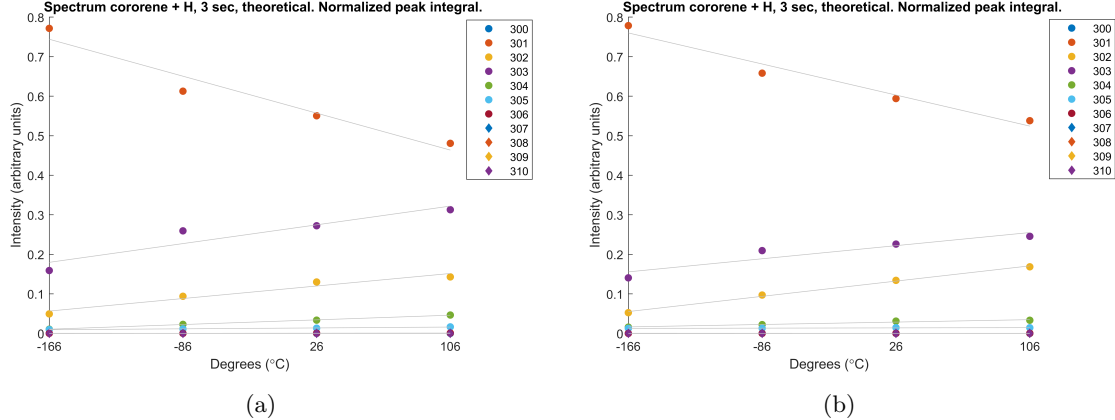


Figure 41: (a)  $0.5 \cdot \frac{Th}{T_0}$  (b)  $0.75 \cdot \frac{Th}{T_0}$

Figure 41 looks a bit more like desired experimental result. Although the theoretical model still needs to be changed more to align with the experimental result. The next step is to see when thermal hopping becomes dominant over quantum tunneling. A first attempt with the above formulae for hopping and tunneling shows that tunneling becomes only dominant at extreme ( $T > 5000\text{K}$ ) temperatures. We therefore have to account for the change of the shape of the potential/barrier. DFT calculations show that this barrier varies from  $0.79\text{\AA}$  to  $1.05\text{\AA}$  in width, with a height of  $0.2\text{eV}$  [6] and show that the transmission coefficient of off by several orders of magnitude. Therefore we change the transmission coefficient turns the potential into a cap parabola [63]

$$P_t(E) \approx e^{-\pi W \sqrt{\frac{2m}{\hbar^2}(U-E)}} \quad (26)$$

Unfortunately, the quantum tunneling only dominates at higher temperatures again. This must be the cause of the width of the energy barrier. The next step would be to find out why the tunneling transmission coefficient is so low.

## 6 Conclusion and list of suggestions

The aim of this research was to find out the energy barrier to cororene and several other molecules. There remain several problems unsolved which are listed below.

### 6.1 Points of improvements

As the effect of temperature on the attachment of atomic hydrogen to cororene is not all that clear, several points of improvement can be made for the researcher that picks up this work:

- Problem: The Teflon tube shows dark fringes on the inside. This could be because it was affected by exceeding  $T_g$  and the subsequent transformation from a hard, “glassy” state to a more viscous state as the polymer chain ensemble loses structure. Despite Teflon being a thermoplastic, if stress was applied to make a rigid connection between the copper and the Teflon exceeds  $T_g$  and then reverts, the expansion will be in the vertical direction only because it is hampered in any other. The dark fringes could also be a shadow cast from outside, so part of the tube became more translucent.
  - Suggestion: Clean the Teflon tube or get a new one. In order to prevent this from happening, do not exceed  $T_g \approx 96^\circ C$  because  $T_g$  is  $116^\circ C$ . To make sure the thermal contact is tight, cool the copper to  $N_2(l)$  temperatures and then tighten it to the Teflon. It can then no longer lose contact but might expand a bit in the vertical direction once heated up.
- Problem: The cororene beam is unstable and hence the spectrum fluctuates a lot.
  - We tried lower and lower concentrations of cororene to see if this solves the problem but it still fluctuates until we arrived at the solution introduced in section 3. The electrospray and the process of Coulomb explosion work better for certain molecules, after looking at spectra for e.g. DNA. Firstly, one could try diluting the sample even further to see if the signal gets more stable. Secondly, a different ionizing agent can be used such as zinc instead of silver.
- Problem: The standard deviation is very big and makes the spectrum before and after the temperature change deviate too much. This is a consequence of an unstable beam. If this cannot be solved, the reliability of the whole experiment drops.
  - If no technical solution presents itself, one has to take more measurements to make sure the standard error ( $= \frac{STD}{\sqrt{N}}$ ) becomes small enough and the average hydrogenation taken before and after the temperature change lie closer to each other.
- Problem: the hydrogen flux and cororene densities are unknown. It is a must these need to be known before analyzing experimental data using code which requires the values of these two variables.

## 7 Acknowledgements

I want to thank the following people:

- Jan Mulder as taking the role of technical supervisor and for his many rigorous lessons on how to mindfully work in a research lab and the important lesson that experimental work is much easier said than done.
- Xin Wang for aiding me and teaching me the experimental set-up operations. Also for answering my many questions.

- Thomas Schlathölter for trying to teach me to be precise and focus and Ronnie Hoekstra for his help with solving many problems.
- Stéphanie Cazaux for her help with the gfortran script with which one can obtain the energy barriers. She provided a lot of theoretical expertise of dealing with the theoretical part of the mass spectrum.
- Amber Kamman and Yahia Mostafa for spending many hours in the lab with me trying to get experimental results.
- The workshop of the University of Groningen, most notably Wigger Jonker for teaching me about the electronics regarding our experimental set-up.
- The rest of the QISD (Quantum Interaction and Structural Dynamics) for giving me a fun time in their research group.

## References

1. Russell, R. W., Soifer, B. T. & Willner, S. P. The 4 to 8 micron spectrum of NGC 7027. en. *The Astrophysical Journal* **217**, L149 (Nov. 1977).
2. Tielens, A. G. G. M. The molecular universe. en. *Reviews of Modern Physics* **85**, 1021–1081 (July 2013).
3. Joblin, C., Leger, A. & Martin, P. Contribution of polycyclic aromatic hydrocarbon molecules to the interstellar extinction curve. en. *The Astrophysical Journal* **393**, L79 (July 1992).
4. Sellgren, K. et al. C60 IN REFLECTION NEBULAE. *The Astrophysical Journal* **722**, L54–L57 (Oct. 2010).
5. Sloan, G. Carbon-rich dust from the asymptotic giant branch to planetary nebulae. en. *Planetary and Space Science* **149**, 32–37 (Dec. 2017).
6. Jones, A. P., Köhler, M., Ysard, N., Bocchio, M. & Verstraete, L. The global dust modelling framework THEMIS. *Astronomy & Astrophysics* **602**, A46 (June 2017).
7. Fu, M. et al. Carbon Dots: A Unique Fluorescent Cocktail of Polycyclic Aromatic Hydrocarbons. en. *Nano Letters* **15**, 6030–6035 (Sept. 2015).
8. Sun, Y., Yang, S., Zhao, G., Wang, Q. & Wang, X. Adsorption of Polycyclic Aromatic Hydrocarbons on Graphene Oxides and Reduced Graphene Oxides. en. *Chemistry - An Asian Journal* **8**, 2755–2761 (Nov. 2013).
9. Samorí, P., Severin, N., Simpson, C. D., Müllen, K. & Rabe, J. P. Epitaxial Composite Layers of Electron Donors and Acceptors from Very Large Polycyclic Aromatic Hydrocarbons. en. *Journal of the American Chemical Society* **124**, 9454–9457 (Aug. 2002).
10. Boschman, L. et al. Hydrogenation of pah cations: a first step toward h2 formation. *The Astrophysical Journal* **761**, L33 (Dec. 2012).
11. Wooden, Charnley & Ehrenfreud. Composition and Evolution of interstellar clouds. *Comets* (Jan. 2004).
12. Maio, U., Dolag, K., Ciardi, B. & Tornatore, L. Metal and molecule cooling in simulations of structure formation. en. *Monthly Notices of the Royal Astronomical Society* **379**, 963–973 (Aug. 2007).
13. Alpher, R. A., Bethe, H. & Gamow, G. The Origin of Chemical Elements. en. *Physical Review* **73**, 803–804 (Apr. 1948).
14. Morris, P. W. et al. HERSCHEL HIFI SPECTRAL MAPPING OF C + , CH + , AND CH IN ORION BN/KL: THE PREVAILING ROLE OF ULTRAVIOLET IRRADIATION IN CH + FORMATION. *The Astrophysical Journal* **829**, 15 (Sept. 2016).
15. Dyson, J. & Williams, D. *The Physics of the Interstellar Medium, Second Edition* en (Taylor & Francis, Jan. 1997).
16. Of Technology, S. U. *Dust Grain Study* online. May 2019.
17. Hollenbach, D. & Salpeter, E. E. Surface Recombination of Hydrogen Molecules. en. *The Astrophysical Journal* **163**, 155 (Jan. 1971).
18. Sternberg, A. & Dalgarno, A. Chemistry in Dense Photon-dominated Regions. en. *The Astrophysical Journal Supplement Series* **99**, 565 (Aug. 1995).
19. Hierl, P. M., Morris, R. A. & Viggiani, A. A. Rate coefficients for the endothermic reactions  $C+(2P)+H_2(D2) \rightarrow CH+(CD+)+H(D)$  as functions of temperature from 400–1300 K. en. *The Journal of Chemical Physics* **106**, 10145–10152 (June 1997).
20. Kramers, H. A. & Ter Haar, D. Condensation in interstellar space. **10**, 137 (Apr. 1946).
21. Scherer, S., Just, T. & Frank, P. High-temprature investigations on pyrolytic reactions of propargyl radicals. en. *Proceedings of the Combustion Institute* **28**, 1511–1518 (Jan. 2000).
22. Cherchneff, I., Barker, J. R. & Tielens, A. G. G. M. Polycyclic aromatic hydrocarbon formation in carbon-rich stellar envelopes. en. *The Astrophysical Journal* **401**, 269 (Dec. 1992).
23. Cherchneff, I. The formation of Polycyclic Aromatic Hydrocarbons in evolved circumstellar environments. *EAS Publications Series* **46**, 177–189 (2011).
24. Frenklach, M., Clary, D. W., Gardiner, W. C. & Stein, S. E. Detailed kinetic modeling of soot formation in shock-tube pyrolysis of acetylene. en. *Symposium (International) on Combustion* **20**, 887–901 (Jan. 1985).
25. Frenklach, M. & Feigelson, E. D. Formation of polycyclic aromatic hydrocarbons in circumstellar envelopes. en. *The Astrophysical Journal* **341**, 372 (June 1989).
26. Snow, T. P. & McCall, B. J. Diffuse Atomic and Molecular Clouds. en. *Annual Review of Astronomy and Astrophysics* **44**, 367–414 (Sept. 2006).
27. Bergin, E. A. & Tafalla, M. Cold Dark Clouds: The Initial Conditions for Star Formation. en. *Annual Review of Astronomy and Astrophysics* **45**, 339–396 (Sept. 2007).
28. Demtröder, W. *Atoms, molecules, and photons: an introduction to atomic-, molecular-, and quantum-physics* (Springer, Berlin ; New York, 2006).
29. De Graauw, T., Haser, L., Beintema, D. & Roelfsma, P. Observing with the ISO Short-Wavelength Spectrometer. **315** (Oct. 1996).
30. Allain, T., Sydney Leach & Sedlmayr, E. Photodestruction of PAHs in the interstellar medium: I. Photodissociation rates for the loss of an acetylenic group. *Astronomy and Astrophysics* **305**, 602 (Dec. 1995).
31. Boschman, L. M. P. V., Hoekstra, R. A. & Rijksuniversiteit Groningen. *Chemistry and photophysics of polycyclic aromatic hydrocarbons in the interstellar medium* English. OCLC: 972391439. PhD thesis (2016).
32. Kuwahata, K., Hama, T., Kouchi, A. & Watanabe, N. Signatures of Quantum-Tunneling Diffusion of Hydrogen Atoms on Water Ice at 10 K. en. *Physical Review Letters* **115** (Sept. 2015).
33. Morfill, G. E. & Scholer, M. *Physical Processes in Interstellar Clouds* English. OCLC: 851379805 (Springer Netherlands, Dordrecht, 1987).
34. Verschuur, G. Galactic life cycle. *Sky & Telescope Magazine*, 379 (Apr. 1992).
35. Rauls, E. & Hornekær, L. Catalyzed Routes to Molecular Hydrogen Formation and Hydrogen Addition Reactions on Neutral Polycyclic Aromatic Hydrocarbons under Interstellar Conditions. en. *The Astrophysical Journal* **679**, 531–536 (May 2008).
36. Foley, N. et al. Molecular hydrogen formation on interstellar PAHs through Eley-Rideal abstraction reactions. en. *Monthly Notices of the Royal Astronomical Society* (June 2018).
37. Cazaux, S. et al. The sequence to hydrogenate coronene cations: A journey guided by magic numbers. en. *Scientific Reports* **6** (Apr. 2016).
38. Rideal, E. K. A note on a simple molecular mechanism for heterogeneous catalytic reactions. en. *Mathematical Proceedings of the Cambridge Philosophical Society* **35**, 130 (Jan. 1939).

39. Rapacioli, M. *et al.* Atomic hydrogen interactions with gas-phase coronene cations: hydrogenation versus fragmentation. en. *Physical Chemistry Chemical Physics* **20**, 22427–22438 (2018).
40. Tielens, A. G. G. M. *The physics and chemistry of the interstellar medium* OCLC: ocm60794229 (Cambridge University Press, Cambridge, 2005).
41. Winter, M. *Hydrogen: radii of atoms and ions* Sept. 2018.
42. Kersevan, R. & ADY, M. *Molflow+* 1990.
43. Vacuum, P. *Basics of Helium Leak Detection with Pfeiffer Vacuum* 2007.
44. Littmarck, S. & Saeidi, F. *COMSOL* Stockholm, 1986.
45. Blundell, S. & Blundell, K. M. *Concepts in thermal physics* 2nd ed. OCLC: ocn430497029 (Oxford University Press, Oxford ; New York, 2010).
46. Schekochihin, A. *Lectures on Kinetic Theory of Gases and Statistical Physics* Dec. 2018.
47. Slevin, J. & Stirling, W. Radio frequency atomic hydrogen beam source. en. *Review of Scientific Instruments* **52**, 1780–1782 (Nov. 1981).
48. Belov, M. E. *et al.* Initial implementation of an electrodynamic ion funnel with fourier transform ion cyclotron resonance mass spectrometry. en. *Journal of the American Society for Mass Spectrometry* **11**, 19–23 (Jan. 2000).
49. March, R. E. in *Encyclopedia of Spectroscopy and Spectrometry* 1000–1009 (Elsevier, 1999).
50. CMS, E. *Using Graphical Tools to Understand Quadrupole Theory* May 2014.
51. Kamas, G. *Time and Frequency User's Manual* 1977.
52. Amato, E. & Blasi, P. Cosmic ray transport in the Galaxy: A review. en. *Advances in Space Research* **62**, 2731–2749 (Nov. 2018).
53. Balmer, J. J. Note on the spectral lines of hydrogen. *Annalen der Physik und Chemie* **25** (1885).
54. *Handbook of plasma processing technology: fundamentals, etching, deposition, and surface interactions* (eds Rossnagel, S. M., Cuomo, J. J. & Westwood, W. D.) (Noyes Publications, Park Ridge, N.J., U.S.A, 1990).
55. Hoekstra, R. *Photons shedding light on electron capture by highly charged ions* PhD thesis (University of Groningen, Mar. 1990).
56. Murray, K. *Reflectron schematic* June 2017.
57. Cotter, R. J. Time-of-flight mass spectrometry for the structural analysis of biological molecules. en. *Analytical Chemistry* **64**, 1027A–1039A (Nov. 1992).
58. Cassler, D. *All About Baluns* June 2017.
59. Chemours. *Fluoroplastic Comparison - Typical Properties*
60. Kirby, R. Thermal Expansion of Polytetrafluoroethylene (Teflon) From -190 to +300 C. *Journal of Research of the National Bureau of Standards* **57** (Aug. 1956).
61. Ling, S., Sanny, J. & Moebs, W. *University Physics* (OpenStax, Rice University).
62. Chaabouni, H. *et al.* Sticking coefficient of hydrogen and deuterium on silicates under interstellar conditions. *Astronomy & Astrophysics* **538**, A128 (Feb. 2012).
63. student, M. & OWB. *Lecture 20: Quantum Tunneling of Electrons* en. 2014.
64. Crowe, M. C. & Campbell, C. T. Adsorption Microcalorimetry: Recent Advances in Instrumentation and Application. en. *Annual Review of Analytical Chemistry* **4**, 41–58 (July 2011).
65. Thompson, W. The physical adsorption of hydrogen on polyethylene and teflon. en. *Physica* **26**, 890–916 (Nov. 1960).
66. Dynamics, D. *Measurement principles of LDA* 2019.

## A Experimental techniques to determine adsorption energy and kinetic energy of H<sub>2</sub>

Here, we present two techniques that were candidates in determining the energy lost per hydrogen per collision with the Teflon walls and in finding out the kinetic energy of the atoms emerging of the Teflon tube. By measuring the first, one could deduce the amount of collisions needed and adapt the length of the Teflon tube part that is cooled to ensure this amount of collisions is needed. Unfortunately, this has not been done for atomic H but only for molecular H, H<sub>2</sub>. The second technique was deemed unsuitable as you would need a laser with a wavelength specific to the Lyman, Balmer or Paschen series.

The first technique is called single crystal calorimetry and aims to calculate the adsorption energy per mole,  $E_0$ . This is shown in figure 42.

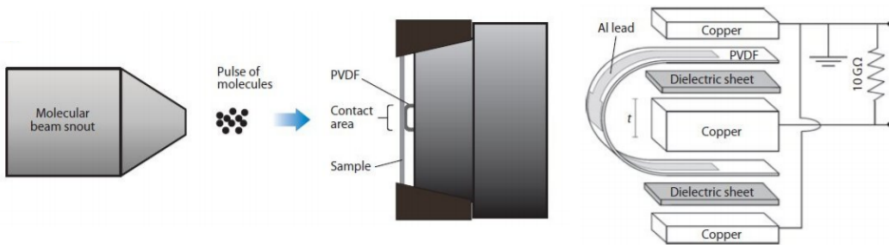


Figure 42: A single crystal calorimetry detector (SCAC) assembly. When a particle impinges on a sample surface, the pyroelectric heat detector (made out of PVDF) measures a change in temperature when a current flows. Source: [64]

In the 1960ies, this method was employed to find the adsorption energy of H<sub>2</sub> upon Teflon for low temperatures and pressures of 20K and 10<sup>-3</sup> mbar. Then, they found an  $E_0$  of 650cal/mole or 2.5kJ/mol [65]. As the boundary between physisorption (interaction dominated by Van der Waals forces) and chemisorption is about the zone between 20kJ/mol and 50kJ/mol respectively, only physisorption takes place in this process.

The second technique d is called Laser Doppler Velocimetry. For this method a laser needs to be installed, including a beam splitter (Bragg cell in figure 43 and a photodetector. The laser is first split and then recombined at the end of the Teflon tube or, even better, just before entering the Paul trap. This creates interference fringes at the recombination point. If the particle then travels through this recombination point it will periodically reflect light in the constructive interference fringes. This light can be collected by the photodetector which will detect a sinusoidal signal. By measuring the frequency of this signal  $f$ , one can calculate the velocity of the particle by applying  $V = d_f \cdot f$ . The fringe spacing  $d_f$  can be found by applying  $d_f = \frac{\lambda}{2\sin(\theta/2)}$  where  $\lambda$  is the wavelength of the laser and  $\theta$  the angle separation between the two beams.

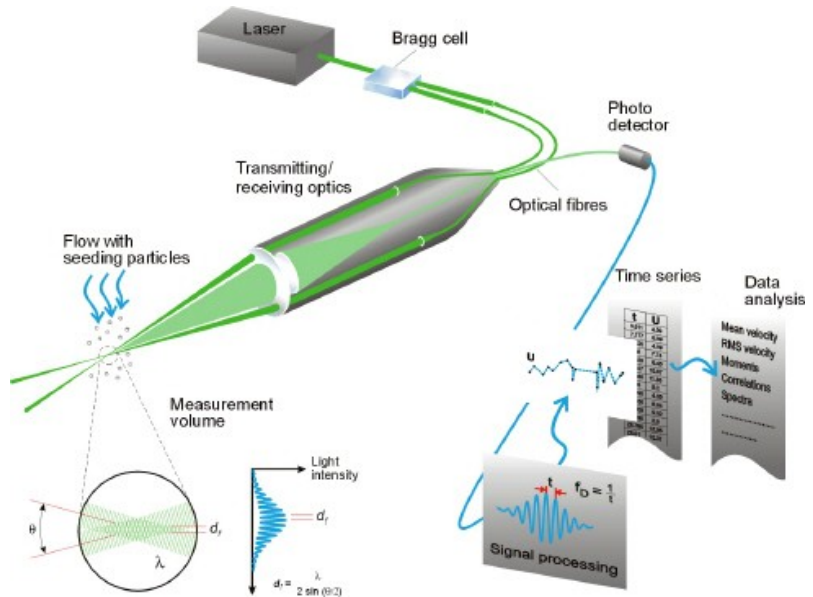


Figure 43: The working principle of Laser Doppler Velocimetry (LDV). The Bragg cell is a piezoelectric transducer attached to a crystal which increasez the frequency of the beam (photons and phonons are conserved in the process). Source: [66]